INTERNATIONAL JOURNAL FOR NUMERICAL METHODS IN ENGINEERING
Int. J. Numer. Meth. Engng 2012; **92**:268–300
Published online 12 June 2012 in Wiley Online Library (wileyonlinelibrary.com). DOI: 10.1002/nme.4336

Partitioned vibration analysis of internal fluid–structure interaction problems

José A. González[1], K. C. Park[2,4,*,†], I. Lee[3], C. A. Felippa[4] and R. Ohayon[5]

[1]*Escuela Superior de Ingenieros, Camino de los Descubrimientos s/n, E-41092 Seville, Spain*
[2]*Division of Ocean Systems Engineering, KAIST, Daejeon 305-701, Korea*
[3]*Division of Aerospace Engineering, KAIST, Daejeon 305-701, Korea*
[4]*Department of Aerospace Engineering Sciences and Center for Aerospace Structures, University of Colorado, Campus Box 429, Boulder, CO 80309, USA*
[5]*Chair of Mechanics, Structural Mechanics and Coupled System Laboratory, Conservatoire National des Arts et Métiers (CNAM), 75003 Paris, France*

SUMMARY

A partitioned, continuum-based, internal fluid–structure interaction (FSI) formulation is developed for modeling combined sloshing, acoustic waves, and the presence of an initial pressurized state. The present formulation and its computer implementation use the method of localized Lagrange multipliers to treat both matching and non-matching interfaces. It is shown that, with the context of continuum Lagrangian kinematics, the fluid sloshing and acoustic stiffness terms originate from an initial pressure term akin to that responsible for geometric stiffness effects in solid mechanics. The present formulation is applicable to both linearized vibration analysis and nonlinear FSI transient analysis provided that a convected kinematics is adopted for updating the mesh geometry in a finite element discretization. Numerical examples illustrate the capability of the present procedure for solving coupled vibration and nonlinear sloshing problems. Copyright © 2012 John Wiley & Sons, Ltd.

Received 11 September 2011; Revised 3 January 2012; Accepted 18 March 2012

KEY WORDS: acoustic waves; gravity waves; sloshing; vibration; fluid–structure interaction; partitioned analysis; localized Lagrange multipliers

1. INTRODUCTION

The problems addressed in this paper have important engineering applications. Examples are liquified natural gas carriers, liquid propellant launchers, fuel tanks in airplanes, satellites and automobiles, large containers under seismic action, and dynamics of trapped water on the deck of offshore vessels and platforms. According to Ibrahim [1], the first reported work on sloshing was by Hough [2], who investigated the dynamics of a rotating ellipsoidal shell containing fluid. Since that early work, sloshing phenomena have remained a major design consideration in the aerospace and naval architecture fields. Interested readers may consult recent monographs and texts [1, 3–5] and review articles [6–8], among others. It should be noted that the bulk of the sloshing problems considered so far deal with rigid containers.

For sloshing motions of fluid in partially filled flexible containers, various formulations and solution methods have been proposed, which include the following: velocity potential for the fluid and modal superposition for the structure [9, 10], Boundary integral for the fluid and modal superposition/FEM for the structure [11–16], Eulerian–Lagrangian equations for the fluid and the finite

*Correspondence to: K. C. Park, Division of Ocean Systems Engineering, KAIST, Daejeon 305-701, Korea.
†E-mail: kcpark@colorado.edu

element/volume method for the structure [17–21], and Lagrangian equation for the fluid with the FEM for the structure [22–27], among others.

When containers are completely filled with fluid and/or gas, fluid–structure interaction (FSI) may be important, which leads to special formulations distinct from sloshing problems [28]. To date, these two problem classes (sloshing-flexible structure interaction and acoustic-flexible structure interaction) have been handled by distinct formulations, resulting in different computer implementations (e.g., [5]).

In addition to the aforementioned fluid and structural formulations issues, to carry out a dynamic interaction analysis, a third issue emerges: *interaction interface treatment* and its computer implementation. For treatment of FSI interfaces, various techniques have been proposed. These range from tightly coupled monolithic schemes to loosely coupled partitioned procedures [17, 20, 21, 23, 29–36].

In developing a partitioned formulation of FSI analysis and after surveying previous work on internal FSI problems, the present authors identified in an earlier work [35] that a more general and computationally modular approach should possess the following desirable attributes. First, formulations and computer implementation for each of the coupled components (fluid and structure in our case) should be stand-alone, with coupling terms modularly separated from each component. Second, the formulation should encompass both sloshing and acoustic phenomena within a unified framework. Third, with the anticipation of highly nonlinear phenomena in the fluid (such as wave breaking and cavitation), the formulation should facilitate interfaces with multi-physics spatial domains. Fourth, should more complex physical effects (for instance, nonlinear surface tension due to high viscosity) be considered, the new coupling effects should be able to be handled via a modified interface treatment procedure while leaving the existing fluid and structure modules largely intact.

One way to meet the preceding desirable features was to employ the partitioned treatment of the interaction interface constraint via the method of localized Lagrange multipliers (LLMs) [37–39]. This choice was largely due to our experience with the LLM method as applied to a variety of problems, in particular to structural mechanics problems. Since we adopt the finite element modeling of flexible structural systems, it was natural to employ a Lagrangian formulation of internal fluid dynamics; such Lagrangian frame pairings, both for structure and fluid, can lead to a simpler construction of interface interaction constraints than pairing of the structural interface displacement to interface velocity potential or interface pressure for the fluid. Hence, a general variational framework can be used to formulate partitioned systems that utilizes the *same kinematic frame* in the fluid–structure interface.

The present paper is organized as follows. After a brief introduction of the problem statement and its variational form of the present partitioned continuum-based formulation in Sections 2 and 3, a detailed continuum-based derivation of Lagrangian fluid equations is presented in Section 4. While the present derivation begins with an earlier continuum-based Lagrangian description of an earlier work [35], several noteworthy refinements and implementation details are presented. First, the surface traction term on the free surface that is often approximated by the Laplace–Young surface tension formula is removed by invoking the equilibrium condition between the free-surface pressure and the traction terms from the continuum variational term. Second, the constitutive relation employed allows both sloshing and acoustic waves, which leads to two distinct fluid stiffness terms: compressibility for acoustic part and incompressibility for the sloshing part. To alleviate *volumetric locking* on the sloshing term, we have employed a mean dilation procedure. Third, a significant item in the present formulation is the manifestation of both acoustic and sloshing stiffness matrices in a form of the so-called *geometric stiffness* that depends on the pressure at each element center. This implies that, when the element nodes are updated in a convected kinematic frame, the present formulation is capable to carry out nonlinear sloshing and acoustic propagation.

Section 5 summarizes the standard FEM formulation of the structure, and Section 6 and 7 present the details of the method of LLMs that establishes the coupling between the fluid and the structure in a partitioned manner. A particular aspect of the LLM method is the use of interface frame whose discretization plays a critical role to pass the frame patch test for convergence of the partitioned equations of motion. This is described in Section 8. The overall partitioned FSI formulation is summarized in Section 9.

DOI: 10.1002/nme

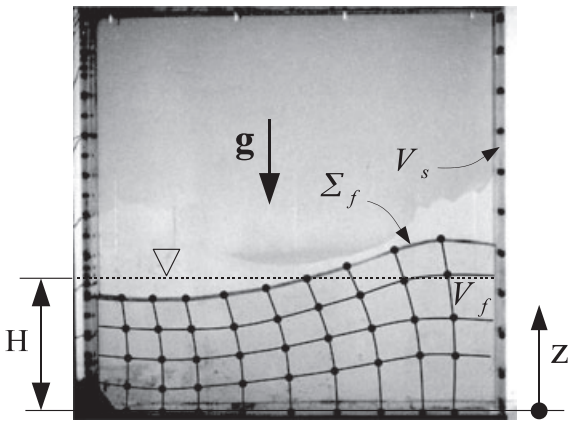

Figure 1. Container with a liquid in motion. Finite elements are used to describe the motion of the fluid with the use of the Lagrangian kinematic description.

Numerical experiments using the present partitioned continuum-based FSI formulation are carried out in Section 10, which illustrate the validity of the present partitioned FSI formulation for linearized structural vibrations due to both acoustic and sloshing phenomena, and nonlinear transient responses. Finally, a discussion of the present study, further refinements, and open problems are offered in Section 11.

2. STATEMENT OF THE PROBLEM

We consider the determination of small amplitude motions of an *inviscid*, *homogeneous*, and *compressible* liquid with a free surface Σ_{f}. The fluid is contained in a linear elastic tank structure, as illustrated in Figure 1. The internal fluid is considered to be initially at rest occupying a volume V_{f} under hydrostatic equilibrium due to the action of the gravity field $\mathbf{g}$. At the same time, the elastic structure containing the liquid occupies a volume V_{s} and presents a *wet surface*, common interface with the fluid denoted by Γ_{b}. The structure is driven by external forces and/or displacements that will produce a coupled oscillation of the two media.

A global reference system $\mathbf{X}(X, Y, Z)$ is introduced with the vertical direction Z and its unit vector $\mathbf{k}$ measured from the bottom of the tank, defining the undisturbed fluid level inside the tank as H. The gravity field is directed along $-Z$. To describe the motion of fluid and structure, we use the displacement fields $\mathbf{u}_{\mathrm{f}}$ and $\mathbf{u}_{\mathrm{s}}$, defined in V_{f} and V_{s}, respectively. Adding to the reference configurations $\mathbf{X}_{\mathrm{f}}$ and $\mathbf{X}_{\mathrm{s}}$ provide the current position vectors $\mathbf{x}_{\mathrm{f}}$ and $\mathbf{x}_{\mathrm{s}}$:

$$\mathbf{x}_{\mathrm{f}} = \mathbf{X}_{\mathrm{f}} + \mathbf{u}_{\mathrm{f}}, \qquad \mathbf{x}_{\mathrm{s}} = \mathbf{X}_{\mathrm{s}} + \mathbf{u}_{\mathrm{s}}, \tag{1}$$

expressed in the global system.

3. PARTITIONED FLUID–STRUCTURE INTERACTION FORMULATION VIA LOCALIZED LAGRANGE MULTIPLIERS

The LLM treatment of the problem is schematized in Figure 2, in which the total FSI system is divided into three subsystems: the fluid, the *interface frame*, and the structure.

To derive the equations of motion for the FSI system, we use the variational formulation proposed by Park and Felippa [37–39], which was later particularized to FSI problems [34, 35]. The virtual work of the coupled system is obtained by adding up the contributions of fluid and structure as if they were independent subsystems and then adding the interface contribution obtained, scaling the constraint equations by the LLMs. It follows that the functional that represents the stationary condition of the total energy of the system $\delta\Pi$ is composed of three terms:

$$\delta\Pi = \delta\Pi_{\mathrm{f}} + \delta\Pi_{\mathrm{s}} + \delta\pi^{\mathrm{f}} = 0 \tag{2}$$

DOI: 10.1002/nme

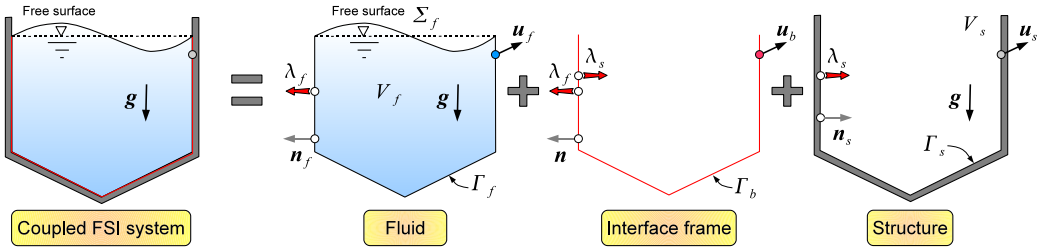

Figure 2. Partitioning of an internal fluid–structure coupled system into three different subsystems: fluid, interface frame, and structure.

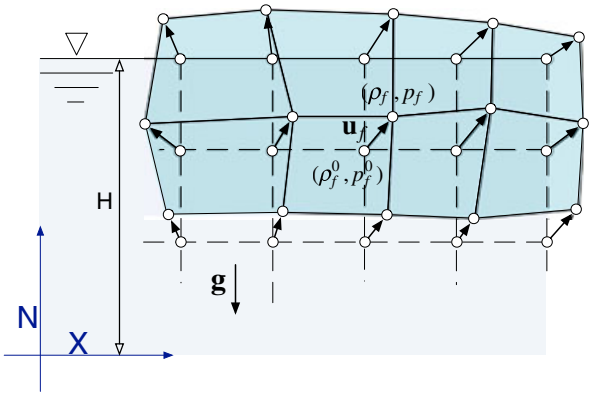

Figure 3. Initial state of the fluid under the action of gravity. Discretization and Lagrangian description of the fluid motion.

where $\delta\Pi_{\mathrm{f}}$ is the virtual work for the fluid, $\delta\Pi_{\mathrm{s}}$ is the virtual work for the flexible structure, and $\delta\pi^{\mathrm{f}}$ is the partition interface constraint that groups contributions from the fluid and the structure. Because $\delta\Pi_{\mathrm{f}} = 0$ and $\delta\Pi_{\mathrm{s}} = 0$ yield the governing equations of motion for the fluid and structure, respectively, the present formulation is able to utilize two independently developed fluid and flexible structural dynamics analysis software modules to perform FSI analysis. These are coupled by an interface treatment module that enforces the interface constraint equations produced by $\delta\pi^{\mathrm{f}} = 0$.

In the following sections, the approximations adopted for each one of these three virtual work expressions are described.

4. FLUID FORMULATION

In the absence of gravity effects, a displacement-based FEM model of an acoustic fluid with no shear stiffness (i.e., inviscid) will experience zero-energy modes. Free rotational modes in the vertical plane disappear when gravity effects are introduced; see [40, 41] for a theoretical derivation.

Because our interest is in FSI, a pure displacement formulation is preferred, where the absence of the pressure will facilitate the connection with the structure.

4.1. Lagrangian description of fluid motion

Let us consider an acoustic fluid under the action of gravity $\mathbf{g}$, initially at rest with density ρ_{f}^0 and hydrostatic pressure due to gravity $p_{\mathrm{f}}^0 = p_{\mathrm{a}} + \rho_{\mathrm{f}}^0 g(H - z)$, where p_{a} is the external atmospheric pressure. Next, assume small deviations from this equilibrium position and introduce a Lagrangian displacement field $\mathbf{u}_{\mathrm{f}}$ following the fluid particle, as represented in Figure 3.

Conservation of mass requires

$$\rho_{\mathrm{f}}^0 = \rho_{\mathrm{f}} J_{\mathrm{f}} \tag{3}$$

with $J_{\mathrm{f}} = \det \mathbf{F}_{\mathrm{f}}$, in which $\mathbf{F}_{\mathrm{f}} = \nabla \mathbf{u}_{\mathrm{f}}$ is the deformation gradient tensor.

DOI: 10.1002/nme

Linearizing the kinematics, the inverse of the fluid dilatation J_f can be approximated as $J_\mathrm{f}^{-1} \approx (1 - \nabla \cdot \mathbf{u}_\mathrm{f})$ and substituted back in (3) to provide a linearized version of mass conservation

$$\rho_\mathrm{f} = \rho_\mathrm{f}^0 (1 - \nabla \cdot \mathbf{u}_\mathrm{f}). \tag{4}$$

On the other hand, for a general equation of state, the speed of sound (c_f) relates the variation of pressure to variation of density in adiabatic conditions, that is,

$$p_\mathrm{f}^{\mathcal{T}} = p_\mathrm{f}^0 + c_\mathrm{f}^2 \left(\rho_\mathrm{f} - \rho_\mathrm{f}^0\right) + \cdots \tag{5}$$

Neglecting all terms involving squares and higher powers of $\left(\rho_\mathrm{f} - \rho_\mathrm{f}^0\right)$, this relation can be substituted in (4) to express the *total fluid pressure* in Lagrangian form as

$$p_\mathrm{f}^{\mathcal{T}} = p_\mathrm{f}^0 - \kappa_\mathrm{f} \nabla \cdot \mathbf{u}_\mathrm{f} \tag{6}$$

an *equation of state*, relating Lagrangian pressure with displacements, where $\kappa_\mathrm{f} = \rho_\mathrm{f}^0 c_\mathrm{f}^2$ is the fluid volumetric stiffness. This approximation is well known and has been extensively used to model fluid motion in the framework of Lagrangian kinematics (e.g., [40–45]).

4.2. Fluid problem in strong form

The strong form of the fluid equations is presented in the following for a pure volumetric continuum by using two alternative descriptions. These are the description with respect to the initial configuration V_f and current configuration v_f of the fluid domain. For the description with respect to the initial configuration, the second *Piola–Kirchhoff* stress tensor $\mathbf{S}_\mathrm{f}$ is used together with the *Green–Lagrangian* strain tensor $\mathbf{E}_\mathrm{f}$, and for the current configuration, the *Cauchy* stress tensor $\boldsymbol{\sigma}_\mathrm{f}$ combined with the symmetric deformation tensor $\mathbf{d}_\mathrm{f}$ is preferred.

Partial differential equations to be satisfied on the fluid domain consist of kinematical relation, local balance of momentum, and the constitutive equation, given by

	Initial configuration:	Current configuration:
Kinematics:	$\mathbf{E}_\mathrm{f} = \frac{1}{2}\left(\mathbf{C}_\mathrm{f} - \mathbf{I}\right)$	$\mathbf{d}_\mathrm{f} = \frac{1}{2}\left(\nabla \mathbf{u}_\mathrm{f} + \nabla^\mathsf{T} \mathbf{u}_\mathrm{f}\right)$
Equilibrium:	$\nabla \cdot (\mathbf{F}_\mathrm{f} \mathbf{S}_\mathrm{f}) + \rho_\mathrm{f}^0 \mathbf{g} = \rho_\mathrm{f}^0 \ddot{\mathbf{u}}_\mathrm{f}$	$\nabla \cdot \boldsymbol{\sigma}_\mathrm{f} + \rho_\mathrm{f} \mathbf{g} = \rho_\mathrm{f} \ddot{\mathbf{u}}_\mathrm{f}$
Constitutive:	$\mathbf{S}_\mathrm{f} = 2\frac{\partial U_\mathrm{f}(J_\mathrm{f})}{\partial \mathbf{C}_\mathrm{f}}$	$\boldsymbol{\sigma}_\mathrm{f} = J_\mathrm{f}^{-1} \mathbf{F}_\mathrm{f} \mathbf{S}_\mathrm{f} \mathbf{F}_\mathrm{f}^\mathsf{T}$

where $\mathbf{C}_\mathrm{f} = \mathbf{F}_\mathrm{f}^\mathsf{T} \mathbf{F}_\mathrm{f}$ is the right *Cauchy–Green* strain tensor and $U_\mathrm{f}(J_\mathrm{f})$ the volumetric strain-energy.

Additionally, the boundary conditions are extended to the complete fluid surface ∂V_f that can be divided in two different regions: the free surface Σ_f and the surface in contact with the structure Γ_f with $\partial V_\mathrm{f} = \Gamma_\mathrm{f} \cup \Sigma_\mathrm{f}$ as represented in Figure 2.

When integrating over the free surface Σ_f, the normal pressure is constant and equal to the atmospheric pressure p_a; thus, we ignore any pressure discontinuity across the air-liquid interface due to surface tension. This approximation holds for waves except ripples with extremely short wavelength [46].

Also, normal displacements and tangential tractions have to be prescribed on Γ_f, leading to the following boundary conditions:

$$\begin{aligned} \mathbf{t}_\mathrm{f} &= -p_\mathrm{a} \mathbf{n}_\mathrm{f} \quad \text{on } \Sigma_\mathrm{f} \\ \mathbf{u}_\mathrm{f} \cdot \mathbf{n}_\mathrm{f} &= \bar{u}_n \quad \text{on } \Gamma_\mathrm{f} \\ \mathbf{t}_\mathrm{f} \cdot \boldsymbol{\tau}_\mathrm{f} &= 0 \quad \text{on } \Gamma_\mathrm{f} \end{aligned}$$

with $\mathbf{n}_\mathrm{f}$ and $\boldsymbol{\tau}_\mathrm{f}$ representing the boundary normal and tangential vectors and $\mathbf{t}_\mathrm{f}$ the surface traction vector in the current configuration.

The necessary variational formulation will be described in the following sections based on a referential and spatial description.

DOI: 10.1002/nme

4.3. Fluid energy functional

The energy functional for the fluid is the total potential energy, written as

$$\Pi_{\mathrm{f}}(\mathbf{u}_{\mathrm{f}}) = \int_{V_{\mathrm{f}}} U_{\mathrm{f}}(J_{\mathrm{f}})\,\mathrm{d}V - \Pi_{\mathrm{f}}^{\mathrm{ext}}(\mathbf{u}_{\mathrm{f}}) \tag{7}$$

where the volumetric strain-energy defined as

$$U_{\mathrm{f}}(J_{\mathrm{f}}) = \frac{1}{2}\kappa_{\mathrm{f}}(J_{\mathrm{f}}-1)^2 \tag{8}$$

is only function of the volumetric deformation with a volumetric stiffness κ_{f}. The potential energy due to external forces, written in *d'Alembert* form with the inertial forces introduced as modified body forces, is expressed as

$$\Pi_{\mathrm{f}}^{\mathrm{ext}}(\mathbf{u}_{\mathrm{f}}) = \int_{V_{\mathrm{f}}} \left(\rho_{\mathrm{f}}^0\mathbf{g} - \rho_{\mathrm{f}}^0\ddot{\mathbf{u}}_{\mathrm{f}}\right)\cdot\mathbf{u}_{\mathrm{f}}\,\mathrm{d}V + \int_{\partial V_{\mathrm{f}}} \mathbf{T}_{\mathrm{f}}\cdot\mathbf{u}_{\mathrm{f}}\,\mathrm{d}A \tag{9}$$

where $\ddot{\mathbf{u}}_{\mathrm{f}}$ is the fluid acceleration, $\mathbf{T}_{\mathrm{f}}$ is the surface traction vector, V_{f} represents the fluid domain, and ∂V_{f} is its physical boundary.

The second *Piola–Kirchhoff* stress tensor is obtained from the strain-energy function

$$\mathbf{S}_{\mathrm{f}} = 2\frac{\partial U_{\mathrm{f}}(J_{\mathrm{f}})}{\partial \mathbf{C}_{\mathrm{f}}} = p_{\mathrm{f}}J_{\mathrm{f}}\mathbf{C}_{\mathrm{f}}^{-1} \tag{10}$$

where

$$p_{\mathrm{f}} = \frac{\partial U_{\mathrm{f}}(J_{\mathrm{f}})}{\partial J_{\mathrm{f}}} = \kappa_{\mathrm{f}}(J_{\mathrm{f}}-1) \tag{11}$$

is the acoustic fluid pressure. The *Cauchy* stress tensor is then obtained from $\mathbf{S}_{\mathrm{f}}$ using the *push forward* operation

$$\boldsymbol{\sigma}_{\mathrm{f}} = J_{\mathrm{f}}^{-1}\mathbf{F}_{\mathrm{f}}\mathbf{S}_{\mathrm{f}}\mathbf{F}_{\mathrm{f}}^{\mathsf{T}} \tag{12}$$

and expressed in the deformed configuration. For an inviscid fluid, $\boldsymbol{\sigma}_{\mathrm{f}}$ presents only hydrostatic component and can be expressed as

$$\boldsymbol{\sigma}_{\mathrm{f}} = p_{\mathrm{f}}\mathbf{I}, \tag{13}$$

a diagonal tensor in the current configuration.

The principle of virtual work comes from the stationarity condition of (7), which, when written in the initial configuration, reads as

$$\delta\Pi_{\mathrm{f}}(\mathbf{u}_{\mathrm{f}},\delta\mathbf{u}_{\mathrm{f}}) = \int_{V_{\mathrm{f}}} \mathbf{S}_{\mathrm{f}}\colon\delta\mathbf{E}_{\mathrm{f}}\,\mathrm{d}V - \delta\Pi_{\mathrm{f}}^{\mathrm{ext}}(\mathbf{u}_{\mathrm{f}},\delta\mathbf{u}_{\mathrm{f}}) \tag{14}$$

$$\delta\Pi_{\mathrm{f}}^{\mathrm{ext}}(\mathbf{u}_{\mathrm{f}},\delta\mathbf{u}_{\mathrm{f}}) = \int_{V_{\mathrm{f}}} \left(\rho_{\mathrm{f}}^0\mathbf{g} - \rho_{\mathrm{f}}^0\ddot{\mathbf{u}}_{\mathrm{f}}\right)\cdot\delta\mathbf{u}_{\mathrm{f}}\,\mathrm{d}V + \int_{\partial V_{\mathrm{f}}} \mathbf{T}_{\mathrm{f}}\cdot\delta\mathbf{u}_{\mathrm{f}}\,\mathrm{d}A \tag{15}$$

expressed in terms of the varied Green–Lagrangian strain $\mathbf{E}_{\mathrm{f}}$ with its conjugate stress measure $\mathbf{S}_{\mathrm{f}}$ and a variation of external energy containing the external traction vector $\mathbf{T}_{\mathrm{f}} = \mathbf{t}_{\mathrm{f}}\frac{\mathrm{d}a}{\mathrm{d}A}$ per unit of initial area.

The next step is to proceed with the linearization of (14) around the initial hydrostatic equilibrium state, to derive the equations of motion for the fluid

$$D\delta\Pi_{\mathrm{f}}(\mathbf{u}_{\mathrm{f}},\delta\mathbf{u}_{\mathrm{f}}) = \int_{V_{\mathrm{f}}} \delta\mathbf{E}_{\mathrm{f}}\colon\boldsymbol{\mathcal{C}}_{\mathrm{f}}\colon D\mathbf{E}_{\mathrm{f}}\,\mathrm{d}V + \int_{V_{\mathrm{f}}} \mathbf{S}_{\mathrm{f}}^{\mathcal{T}}\colon\left[\nabla_0^{\mathsf{T}}\mathbf{u}_{\mathrm{f}}\nabla_0\delta\mathbf{u}_{\mathrm{f}}\right]\mathrm{d}V - D\delta\Pi_{\mathrm{f}}^{\mathrm{ext}} \tag{16}$$

DOI: 10.1002/nme

where it is important to note that $\mathbf{u}_\mathrm{f}$ now represents a displacement from equilibrium, as represented in Figure 3. We can identify in the first volume integral the constitutive term that gives place to the constitutive stiffness matrix, with a Lagrangian constitutive tensor given by

$$\mathcal{C}_\mathrm{f} = \mathcal{C}_p + \mathcal{C}_\kappa \tag{17}$$

$$\mathcal{C}_p = p_\mathrm{f} J_\mathrm{f} \left[\mathbf{C}_\mathrm{f}^{-1} \otimes \mathbf{C}_\mathrm{f}^{-1} - 2\mathcal{I}_\mathrm{f}\right] \quad , \quad \mathcal{C}_\kappa = \kappa_\mathrm{f} J_\mathrm{f}^2 \mathbf{C}_\mathrm{f}^{-1} \otimes \mathbf{C}_\mathrm{f}^{-1}$$

where $\mathcal{C}_p$ comes from the variation of kinematic variables and $\mathcal{C}_\kappa$ from the variation of pressure. Second volume integral represents the initial-stress term, which now includes the initial hydrostatic pressure configuration of the fluid.

The linearized equations of motion (16) can be expressed in the current configuration with a similar form

$$D\delta\Pi_\mathrm{f}(\mathbf{u}_\mathrm{f}, \delta\mathbf{u}_\mathrm{f}) = \int_{v_\mathrm{f}} \delta\mathbf{d}_\mathrm{f} \colon \boldsymbol{c}_\mathrm{f} \colon \mathbf{d}_\mathrm{f} \, \mathrm{d}v + \int_{v_\mathrm{f}} p_\mathrm{f}^{\mathcal{T}} \mathbf{I} \colon \left[\boldsymbol{\nabla}^\mathsf{T} \mathbf{u}_\mathrm{f} \boldsymbol{\nabla} \delta\mathbf{u}_\mathrm{f}\right] \mathrm{d}v - D\delta\Pi_\mathrm{f}^\mathrm{ext} \tag{18}$$

using the spatial Cauchy stress $\boldsymbol{\sigma}_\mathrm{f}$ and deformation $\mathbf{d}_\mathrm{f}$ work conjugate tensors, together with the fourth-order constitutive tensor

$$\boldsymbol{c}_\mathrm{f} = \boldsymbol{c}_p + \boldsymbol{c}_\kappa \tag{19}$$

$$\boldsymbol{c}_p = p_\mathrm{f}[\mathbf{I} \otimes \mathbf{I} - 2\boldsymbol{i}] \quad , \quad \boldsymbol{c}_\kappa = \kappa_\mathrm{f} J_\mathrm{f} \mathbf{I} \otimes \mathbf{I}$$

with $\mathbf{I} \otimes \mathbf{I} = \delta_{ij}\delta_{kl}$ and $\boldsymbol{i} = \frac{1}{2}(\delta_{ik}\delta_{jl} + \delta_{il}\delta_{jk})$. In the current configuration, the initial-stress term contains the total Lagrangian pressure $p_\mathrm{f}^{\mathcal{T}} = p_\mathrm{f}^0 + p_\mathrm{f}$.

Linearization of the external virtual work (15) provides

$$D\delta\Pi_\mathrm{f}^\mathrm{ext}(\mathbf{u}_\mathrm{f}, \delta\mathbf{u}_\mathrm{f}) = -\int_{v_\mathrm{f}} \rho_\mathrm{f} \ddot{\mathbf{u}}_\mathrm{f} \cdot \delta\mathbf{u}_\mathrm{f} \, \mathrm{d}v + D\left(\int_{\partial v_\mathrm{f}} \mathbf{t}_\mathrm{f} \cdot \delta\mathbf{u}_\mathrm{f} \, \mathrm{d}a\right) \tag{20}$$

where gravitational body forces, initially present in (15), are invariably independent of the motion and consequently do not contribute to the linearized virtual work. Hence, only inertia forces and external tractions are present in the linearized virtual work because of external forces.

The second term in (20), because of externals tractions, has to be extended first to the free surface Σ_f according to the boundary conditions. Assuming that the fluid displacements are small and that the final configuration coincides with the reference configuration, derivatives of the normal vector can be neglected and the following approximation holds

$$D\left(\int_{\Sigma_\mathrm{f}} \mathbf{t}_\mathrm{f} \cdot \delta\mathbf{u}_\mathrm{f} \, \mathrm{d}a\right) = -\int_{\Sigma_\mathrm{f}} p_a D\mathbf{n}_\mathrm{f} \cdot \delta\mathbf{u}_\mathrm{f} \, \mathrm{d}a \approx 0. \tag{21}$$

Finally, the constraint along the surface in contact with the structure Γ_f is to present the same normal displacement than the structure, combined with zero traction in the tangential direction due to the inviscid property of the fluid.

4.4. Mean dilatation method for incompressibility

A purely kinematic finite element discretization of (16) or (18) is unfortunately not applicable to simulations involving incompressible or quasi-incompressible behavior. It is well known that without further development, previous formulation is over-constrained, resulting in the phenomenon known as *volumetric locking*. Well-known solutions to this problem are as follows: to impose the incompressibility condition by penalization or by using reduced integration methods [47–50], to adopt an augmented Lagrangian formulation enforcing quasi-incompressibility condition [51, 52], or to use u–p elements that satisfy the inf–sup condition [53, 54]. Among all these possibilities, a total displacement formulation with variational treatment of near incompressibility is preferred in order to facilitate the treatment of the interface without sacrificing the benefits of a theory.

DOI: 10.1002/nme

The three-field canonical functional of linear elastostatics identified as the *Veubeke–Hu–Washizu* (VHW) functional in the literature [55,56] will be applied to treat near-incompressibility of the fluid. In this functional, three different interior fields (displacements, stresses, and strains) are defined and independently varied.

In our case, the VHW functional for the fluid uses independent kinematic descriptions for the volumetric and distortional deformation, introducing a new kinematic variable ($\bar{J}_\mathrm{f}$) representing the dilatation independent of $\mathbf{u}_\mathrm{f}$ and a Lagrange multiplier ($\bar{p}_\mathrm{f}$) to enforce the condition $\bar{J}_\mathrm{f} = J_\mathrm{f}(\mathbf{u}_\mathrm{f})$.

The VHW principle applied to energy potential (7) (e.g., [57,58]) states that

$$\Pi_\mathrm{f}^{\mathrm{VHW}}\left(\mathbf{u}_\mathrm{f}, \bar{J}_\mathrm{f}, \bar{p}_\mathrm{f}\right) = \int_{V_\mathrm{f}} U_\mathrm{f}\left(\bar{J}_\mathrm{f}\right)\, \mathrm{d}V + \int_{V_\mathrm{f}} \bar{p}_\mathrm{f}\left(J_\mathrm{f} - \bar{J}_\mathrm{f}\right)\, \mathrm{d}V - \Pi_\mathrm{f}^{\mathrm{ext}}(\mathbf{u}_\mathrm{f}) \tag{22}$$

where $U_\mathrm{f}\left(\bar{J}_\mathrm{f}\right)$ represents the mean volumetric strain-energy. The stationary conditions for (22) are

$$\int_{V_\mathrm{f}} \left(\frac{\partial U_\mathrm{f}\left(\bar{J}_\mathrm{f}\right)}{\partial \bar{J}_\mathrm{f}} - \bar{p}_\mathrm{f} \right) \delta \bar{J}_\mathrm{f}\, \mathrm{d}V = 0 \tag{23}$$

$$\int_{V_\mathrm{f}} \left(J_\mathrm{f} - \bar{J}_\mathrm{f}\right) \delta \bar{p}_\mathrm{f}\, \mathrm{d}V = 0. \tag{24}$$

The mean dilatation approach (equivalent to selective integration) assumes that $\left(\bar{p}_\mathrm{f}, \bar{J}_\mathrm{f}\right)$ and $\left(\delta \bar{p}_\mathrm{f}, \delta \bar{J}_\mathrm{f}\right)$ are constant over the integration volume V_f. Equations (23) and (24) reduce to

$$\bar{p}_\mathrm{f} = \kappa_\mathrm{f}\left(\bar{J}_\mathrm{f} - 1\right) \tag{25}$$

$$\bar{J}_\mathrm{f} = \frac{1}{V_\mathrm{f}} \int_{V_\mathrm{f}} J_\mathrm{f}\, \mathrm{d}V \tag{26}$$

conditions that will be incorporated in our finite element formulation for the fluid.

Applying the mean dilatation method on an arbitrary volume, combining equations (25), (26) and (18), after linearization and transforming to the current configuration [57], gives

$$\begin{aligned} D\delta\bar{\Pi}_\mathrm{f}(\mathbf{u}_\mathrm{f}, \delta\mathbf{u}_\mathrm{f}) = &\int_{v_\mathrm{f}} \mathbf{d}_\mathrm{f} \colon \boldsymbol{c}_p \colon \delta\mathbf{d}_\mathrm{f}\, \mathrm{d}v + \int_{v_\mathrm{f}} p_\mathrm{f}^{\mathcal{T}}\mathbf{I} \colon \left[\boldsymbol{\nabla}^{\mathsf{T}}\mathbf{u}_\mathrm{f}\boldsymbol{\nabla}\delta\mathbf{u}_\mathrm{f}\right]\, \mathrm{d}v \\ &+ \mathcal{K}_\mathrm{f} v_\mathrm{f} \int_{v_\mathrm{f}} \boldsymbol{\nabla}\cdot\mathbf{u}_\mathrm{f}\, \mathrm{d}v \int_{v_\mathrm{f}} \boldsymbol{\nabla}\cdot\delta\mathbf{u}_\mathrm{f}\, \mathrm{d}v + \int_{v_\mathrm{f}} \rho_\mathrm{f}\ddot{\mathbf{u}}_\mathrm{f}\cdot\delta\mathbf{u}_\mathrm{f}\, \mathrm{d}v \end{aligned} \tag{27}$$

where $\mathcal{K}_\mathrm{f} = \kappa_\mathrm{f}\frac{v_\mathrm{f}}{V_\mathrm{f}}$ is the fluid volumetric stiffness in the current configuration and because the fluid pressure $\bar{p}_\mathrm{f}$ is constant over volume v_f, the fourth-order constitutive tensor $\boldsymbol{c}_\mathrm{f}$ only presents the pressure term $\boldsymbol{c}_p$.

4.5. Discrete approximation of fluid functional

The mean dilatation approach for a given volume V_f leads to a constant pressure over that volume, as indicated by equations (25) and (26). When this formulation is applied to an individual fluid element identified by superscript (e) in a finite element mesh, the acoustic pressure becomes constant over the element volume. In particular, considering (26) in an element with volume $V_\mathrm{f}^{(e)}$ together with the linearization $J_\mathrm{f} \approx (1 + \boldsymbol{\nabla}\cdot\mathbf{u}_\mathrm{f})$, the element dilatation average is

$$\left(\bar{\boldsymbol{\nabla}}\cdot\mathbf{u}_\mathrm{f}\right)^{(e)} = \frac{1}{V_\mathrm{f}^{(e)}} \int_{V_\mathrm{f}^{(e)}} \boldsymbol{\nabla}\cdot\mathbf{u}_\mathrm{f}\, \mathrm{d}V. \tag{28}$$

By using the expression of uniform acoustic pressure given by equation (25) at the element level, the uniform element acoustic pressure becomes

$$\bar{p}_\mathrm{f}^{(e)} = \kappa_\mathrm{f}\left(\bar{\boldsymbol{\nabla}}\cdot\mathbf{u}_\mathrm{f}\right)^{(e)}, \tag{29}$$

DOI: 10.1002/nme

in which acoustic pressure $\bar{p}_{\mathrm{f}}^{(e)}$ is constant inside the element. Next, recall the linearized virtual work equation (27), which for an element (e) is

$$D\delta\Pi_{\mathrm{f}}^{(e)} = \int_{V_{\mathrm{f}}^{(e)}} \mathbf{d}_{\mathrm{f}} : \boldsymbol{c}_p : \delta\mathbf{d}_{\mathrm{f}} \, \mathrm{d}V + \int_{V_{\mathrm{f}}^{(e)}} p_{\mathrm{f}}^{\mathcal{T}} \mathbf{I} : \left(\nabla^{\mathsf{T}}\mathbf{u}_{\mathrm{f}} \nabla\delta\mathbf{u}_{\mathrm{f}}\right) \mathrm{d}V + \int_{V_{\mathrm{f}}^{(e)}} \kappa_{\mathrm{f}} (\nabla\cdot\mathbf{u}_{\mathrm{f}})(\nabla\cdot\delta\mathbf{u}_{\mathrm{f}}) \, \mathrm{d}V + \int_{V_{\mathrm{f}}^{(e)}} \rho_{\mathrm{f}}^{0} \ddot{\mathbf{u}}_{\mathrm{f}} \cdot \delta\mathbf{u}_{\mathrm{f}} \, \mathrm{d}V \tag{30}$$

and apply the mean dilatation approach. Because the mean acoustic pressure $\bar{p}_{\mathrm{f}} = \kappa_{\mathrm{f}} \left(\bar{\nabla}\cdot\mathbf{u}_{\mathrm{f}}\right)$ is constant over the element volume, the third volume integral becomes

$$D\delta\Pi_{\mathrm{f}}^{(e)} = \int_{V_{\mathrm{f}}^{(e)}} \mathbf{d}_{\mathrm{f}} : \boldsymbol{c}_p : \delta\mathbf{d}_{\mathrm{f}} \, \mathrm{d}V + \int_{V_{\mathrm{f}}^{(e)}} p_{\mathrm{f}}^{\mathcal{T}} \mathbf{I} : \left(\nabla^{\mathsf{T}}\mathbf{u}_{\mathrm{f}} \nabla\delta\mathbf{u}_{\mathrm{f}}\right) \mathrm{d}V + \kappa_{\mathrm{f}} V_{\mathrm{f}}^{(e)} (\bar{\nabla}\cdot\mathbf{u}_{\mathrm{f}})^{(e)} (\bar{\nabla}\cdot\delta\mathbf{u}_{\mathrm{f}})^{(e)} + \int_{V_{\mathrm{f}}^{(e)}} \rho_{\mathrm{f}}^{0} \ddot{\mathbf{u}}_{\mathrm{f}} \cdot \delta\mathbf{u}_{\mathrm{f}} \, \mathrm{d}V. \tag{31}$$

This is a linearized approximation around the initial hydrostatic equilibrium state, assuming that the fluid deviations from equilibrium are small. Note that in the second initial-stress term appears the total pressure and that the third acoustic term is pure volumetric.

Element displacements are discretized as $\mathbf{u}_{\mathrm{f}} = \mathbf{N}\mathbf{u}_{\mathrm{f}}^{(e)}$, where $\mathbf{N}_{\mathrm{f}}$ collects the element shape functions while $\mathbf{u}_{\mathrm{f}}^{e}$ gathers nodal values of the element. The element stiffness matrix is then composed of three terms:

$$\mathbf{K}^{(e)} = \mathbf{K}_{\mathrm{con}}^{(e)} + \mathbf{K}_{\mathrm{geo}}^{(e)} + \mathbf{K}_{\mathrm{ac}}^{(e)}, \tag{32}$$

$$\mathbf{K}_{\mathrm{con}}^{(e)} = \int_{V_{\mathrm{f}}^{(e)}} \mathbf{B}_{\mathrm{f}}^{\mathsf{T}} \mathbf{C}_p \mathbf{B}_{\mathrm{f}} \, \mathrm{d}V \tag{33}$$

$$\mathbf{K}_{\mathrm{ac}}^{(e)} = \frac{\kappa_{\mathrm{f}}}{V_{\mathrm{f}}^{(e)}} \int_{V_{\mathrm{f}}^{(e)}} (\nabla\cdot\mathbf{N}_{\mathrm{f}})^{\mathsf{T}} \, \mathrm{d}V \int_{V_{\mathrm{f}}^{(e)}} (\nabla\cdot\mathbf{N}_{\mathrm{f}}) \, \mathrm{d}V \tag{34}$$

$$\mathbf{K}_{\mathrm{geo}}^{(e)} = \int_{V_{\mathrm{f}}^{(e)}} p_{\mathrm{f}}^{\mathcal{T}} (\nabla\mathbf{N}_{\mathrm{f}})^{\mathsf{T}} (\nabla\mathbf{N}_{\mathrm{f}}) \, \mathrm{d}V. \tag{35}$$

where $\mathbf{C}_p$ is the spatial constitutive matrix constructed from the fourth-order tensor $\boldsymbol{c}_p$ and $\mathbf{B}_{\mathrm{f}}$ is the deformation matrix.

Here, $\mathbf{K}_{\mathrm{con}}^{(e)}$ is the constitutive stiffness matrix, $\mathbf{K}_{\mathrm{ac}}^{(e)}$ is the acoustic stiffness matrix, whereas $\mathbf{K}_{\mathrm{geo}}^{(e)}$ is the geometrical stiffness matrix. By starting our analysis from an equilibrium configuration where acoustic pressure p_{f} is zero and total pressure $p_{\mathrm{f}}^{\mathcal{T}}$ coincides with initial pressure p_{f}^{0}, assuming small acoustic-pressure oscillations, the constitutive constitutive stiffness matrix (33) can be neglected and the geometrical stiffness (35) evaluated at the initial hydrostatic state p_{f}^{0}.

Spectral analysis of the resultant stiffness matrix for an eight-node, 24 degree-of-freedom (DOF), brick element with a regular (cubic-like) geometry under exact $2 \times 2 \times 2$ integration reveals full rank of 18 with six zero-energy modes corresponding to rigid-body motions. The acoustic stiffness matrix (34) contributes to the rank with one purely volumetric mode, whereas the geometrical stiffness matrix (35) brings the remaining 17 non-zero-energy modes that include shear, torsion, and filling modes.

On the other hand, inertia forces are modeled using the classical element mass matrix

$$\mathbf{M}^{(e)} = \int_{V_{\mathrm{f}}^{(e)}} \rho_{\mathrm{f}}^{0} \mathbf{N}_{\mathrm{f}}^{\mathsf{T}} \mathbf{N}_{\mathrm{f}} \, \mathrm{d}V. \tag{36}$$

Upon assembling the element matrices, we arrive to the matrix form of the first variation for the complete fluid mesh

$$\delta\Pi_{\mathrm{f}} = \delta\mathbf{u}_{\mathrm{f}}^{\mathsf{T}} \{\mathbf{M}_{\mathrm{f}}\ddot{\mathbf{u}}_{\mathrm{f}} + \mathbf{K}_{\mathrm{f}}\mathbf{u}_{\mathrm{f}} - \mathbf{f}_{\mathrm{f}}\} \tag{37}$$

DOI: 10.1002/nme

in which $\mathbf{M}_\mathrm{f}$ and $\mathbf{K}_\mathrm{f}$ are the mass and stiffness matrices of the fluid, respectively; $\mathbf{u}_\mathrm{f}$ the vector of fluid node displacements; and $\mathbf{f}_\mathrm{f}$ the applied node force vector, zero in our case. As we can see, the second-order Ordinary Differential Equation (ODE) representing the fluid equations of motion is only a function of displacements and its time derivatives.

5. STRUCTURE FORMULATION

The structure is described by the well-known equations of motion for an elastic body modeled as a continuum. Because fluid motions were assumed small, a similar consideration is taken for the structure. To this end, we write directly the variational formulation of the structural model as

$$\delta\Pi_\mathrm{s}(\mathbf{u}_\mathrm{s}, \delta\mathbf{u}_\mathrm{s}) = \int_{V_\mathrm{s}} \boldsymbol{\sigma}_\mathrm{s} \colon \nabla\delta\mathbf{u}_\mathrm{s}\, \mathrm{d}V - \int_{\partial V_\mathrm{s}} \mathbf{t}_\mathrm{s} \cdot \delta\mathbf{u}_\mathrm{s}\, \mathrm{d}A + \int_{V_\mathrm{s}} \rho_\mathrm{s}\ddot{\mathbf{u}}_\mathrm{s} \cdot \delta\mathbf{u}_\mathrm{s}\, \mathrm{d}V \tag{38}$$

where $\mathbf{u}_\mathrm{s}$, $\boldsymbol{\sigma}_\mathrm{s}$, and $\mathbf{t}_\mathrm{s}$ denote structural displacements, stresses, and surface tractions, respectively.

Considering that the external surface of the structure ∂V_s is divided in wet Γ_s and dry Σ_s boundaries, the boundary conditions on the wet surface Γ_s present a displacement restriction in the normal direction, same normal displacement than the fluid, and a zero-traction condition in the tangential direction. Finally, it is assumed that external tractions are only applied on Σ_s,

$$\int_{\partial V_\mathrm{s}} \mathbf{t}_\mathrm{s} \cdot \delta\mathbf{u}_\mathrm{s}\, \mathrm{d}A = \int_{\Sigma_\mathrm{s}} \mathbf{t}_\mathrm{s} \cdot \delta\mathbf{u}_\mathrm{s}\, \mathrm{d}A \tag{39}$$

term that results, after discretization, in an external force vector.

5.1. Discrete approximation of structure functional

The structure is spatially discretized using the classical FEM approach. The assembly of element contributions by the direct stiffness method leads to the semidiscrete equations of motion

$$\delta\Pi_\mathrm{s} = \delta\mathbf{u}_\mathrm{s}^\mathsf{T}\{\mathbf{M}_\mathrm{s}\ddot{\mathbf{u}}_\mathrm{s} + \mathbf{K}_\mathrm{s}\mathbf{u}_\mathrm{s} - \mathbf{f}_\mathrm{s}\} \tag{40}$$

in which $\mathbf{M}_\mathrm{s}$ and $\mathbf{K}_\mathrm{s}$ are the mass and stiffness matrices, respectively; $\mathbf{u}_\mathrm{s}$ the vector of node displacements; and $\mathbf{f}_\mathrm{s}$ the applied node force vector.

6. INTERFACE FRAME

To formulate the interface problem, instead of considering the direct interaction between the fluid and the structure, we insert between them a deforming non-physical surface or *interface frame* denoted as Γ_b. The FSI problem is reformulated in terms of interaction of the fluid and structure partitions with this auxiliary surface by using LLMs collocated on each side of the frame.

The interaction forces acting on the frame are depicted in Figure 4. The LLMs connecting the fluid volume V_f with the frame are denoted by $\boldsymbol{\lambda}_\mathrm{f} = \{\lambda_{f_n}, \lambda_{f_{t_1}}, \lambda_{f_{t_2}}\}^\mathsf{T}$, whereas multipliers connecting the structure V_s with the frame are $\boldsymbol{\lambda}_\mathrm{s} = \{\lambda_{s_n}, \lambda_{s_{t_1}}, \lambda_{s_{t_2}}\}^\mathsf{T}$. These forces are expressed using a local orthonormal base system attached to the frame, $\mathbf{B} = [\mathbf{n}, \mathbf{t}_1, \mathbf{t}_2]$, that depends of the position occupied by the node on the frame and that is used to describe $\boldsymbol{\lambda}_\mathrm{f}$ and $\boldsymbol{\lambda}_\mathrm{s}$. This frame local system is defined by convention in the following way; $\mathbf{t}_1$ and $\mathbf{t}_2$ are the orthogonal vectors contained in the frame tangent plane at the considered point $\boldsymbol{\xi}_p$, and vector $\mathbf{n}$ points towards structure V_s.

6.1. Frame kinematics

The motion of the interface frame is described using a displacement field $\mathbf{u}_b = \{u_{b_n}, u_{b_{t_1}}, u_{b_{t_2}}\}^\mathsf{T}$ and its initial configuration $\mathbf{X}_b$, providing a current position,

$$\mathbf{x}_b = \mathbf{X}_b + \mathbf{u}_b, \tag{41}$$

DOI: 10.1002/nme

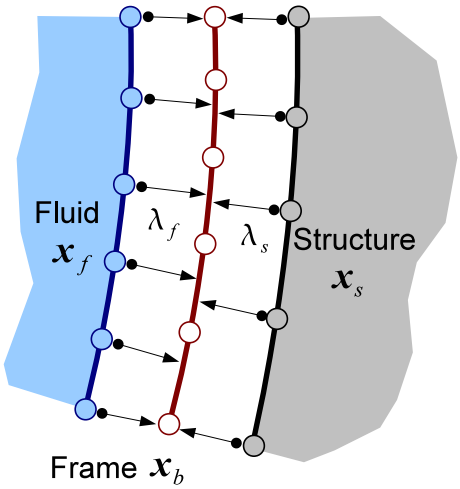

Figure 4. Treatment of non-matching interfaces using localized Lagrange multipliers. The fields of multipliers on the fluid side $\boldsymbol{\lambda}_{\mathrm{f}}$ and the structural side $\boldsymbol{\lambda}_{\mathrm{s}}$ are discretized using Dirac delta functions collocated at the nodes. If the fluid is inviscid, only normal displacements of the frame and normal components of these multipliers are considered.

that is restricted to follow the fluid–structure interface. To do so, the frame–fluid and frame–structure relative displacements are required to vanish. These conditions are expressed in the frame local system as

$$\mathbf{B}^{\mathsf{T}}(\mathbf{x}_{\mathrm{f}} - \mathbf{x}_b) = \mathbf{0}, \qquad \mathbf{B}^{\mathsf{T}}(\mathbf{x}_{\mathrm{s}} - \mathbf{x}_b) = \mathbf{0}, \tag{42}$$

and extended to the fluid interface Γ_{f} and the structure interface Γ_{s}, respectively. If the fluid is inviscid, the tangential stress on the wall is zero. Thus, the tangential displacements of the fluid and the structure at Γ_{f} become independent. In this case, only the kinematic condition of (42) in the normal direction applies, that is,

$$\mathbf{n}^{\mathsf{T}} \cdot (\mathbf{x}_{\mathrm{f}} - \mathbf{x}_b) = 0, \qquad \mathbf{n}^{\mathsf{T}} \cdot (\mathbf{x}_{\mathrm{s}} - \mathbf{x}_b) = 0. \tag{43}$$

This simplification reduces the displacement field on the frame to $\mathbf{u}_b = \{u_b\}$ with only one component in the normal direction, whereas the LLMs of the fluid and structure side reduce to $\boldsymbol{\lambda}_{\mathrm{f}} = \{\lambda_n\}$ and $\boldsymbol{\lambda}_{\mathrm{s}} = \{\lambda_{\mathrm{s}}\}$, respectively.

7. VARIATIONALLY BASED INTERFACE COUPLING

Use of a variational formulation to treat the fluid–structure connection possesses the significant advantage of preserving the symmetry of the equations of motion. In the present section, the variational framework described in [35] is used to obtain the interface coupling equations.

7.1. Interface constraint functional

Consider the fluid–structure boundary Γ_b shown in Figure 4, in which the interface frame carries an independent field of displacements ($\mathbf{u}_b$). The fluid boundary displacements ($\mathbf{u}_{\mathrm{f}}$), the structure boundary displacements ($\mathbf{u}_{\mathrm{s}}$), as well as their associated multipliers on the fluid ($\boldsymbol{\lambda}_{\mathrm{f}}$) and the structure ($\boldsymbol{\lambda}_{\mathrm{s}}$) will appear in the variational formulation of the interaction conditions. The interface functional variation splits into contributions from fluid and structure:

$$\delta\pi^{\mathrm{f}} = \delta\pi_{\mathrm{f}}^{\mathrm{int}} + \delta\pi_{\mathrm{s}}^{\mathrm{int}} \tag{44}$$

DOI: 10.1002/nme

To construct the interface functional for the fluid, the kinematic constraint equation (42) is enforced in a weak sense using the fluid-side multipliers:

$$\delta\pi_{\mathrm{f}}^{\mathrm{int}} = \int_{\Gamma_{\mathrm{b}}} \delta\left\{\boldsymbol{\lambda}_{\mathrm{f}} \cdot \left[\mathbf{B}^{\mathsf{T}}(\mathbf{x}_{\mathrm{f}} - \mathbf{x}_b)\right]\right\} \mathrm{d}A. \tag{45}$$

This is integrated by parts to provide the total variation of the interface potential on the fluid side,

$$\delta\pi_{\mathrm{f}}^{\mathrm{int}} = \int_{\Gamma_{\mathrm{b}}} \left(\boldsymbol{\lambda}_{\mathrm{f}} \cdot \delta\left\{\mathbf{B}^{\mathsf{T}}(\mathbf{x}_{\mathrm{f}} - \mathbf{x}_b)\right\} + \delta\boldsymbol{\lambda}_{\mathrm{f}} \cdot \left\{\mathbf{B}^{\mathsf{T}}(\mathbf{x}_{\mathrm{f}} - \mathbf{x}_b)\right\}\right) \mathrm{d}A. \tag{46}$$

Likewise, for the structure side,

$$\delta\pi_{\mathrm{s}}^{\mathrm{int}} = \int_{\Gamma_{\mathrm{b}}} \left(\boldsymbol{\lambda}_{\mathrm{s}} \cdot \delta\left\{\mathbf{B}^{\mathsf{T}}(\mathbf{x}_{\mathrm{s}} - \mathbf{x}_b)\right\} + \delta\boldsymbol{\lambda}_{\mathrm{s}} \cdot \left\{\mathbf{B}^{\mathsf{T}}(\mathbf{x}_{\mathrm{s}} - \mathbf{x}_b)\right\}\right) \mathrm{d}A. \tag{47}$$

To deal with the first term of equations (46) and (47) we use the decomposition

$$\boldsymbol{\lambda}_{\mathrm{f}} \cdot \delta\left\{\mathbf{B}^{\mathsf{T}}(\mathbf{x}_{\mathrm{f}} - \mathbf{x}_b)\right\} = (\delta\mathbf{u}_{\mathrm{f}} - \delta\mathbf{u}_b) \cdot \{\mathbf{B}\boldsymbol{\lambda}_{\mathrm{f}}\}, \tag{48}$$

$$\boldsymbol{\lambda}_{\mathrm{s}} \cdot \delta\left\{\mathbf{B}^{\mathsf{T}}(\mathbf{x}_{\mathrm{s}} - \mathbf{x}_b)\right\} = (\delta\mathbf{u}_{\mathrm{s}} - \delta\mathbf{u}_b) \cdot \{\mathbf{B}\boldsymbol{\lambda}_{\mathrm{s}}\}, \tag{49}$$

which is a first-order approximation in which the variations of the normal and tangential frame unitary vectors are considered to be very small. Substitution into (46) and (47) yields the interface potential for the fluid and structure:

$$\delta\pi_{\mathrm{f}}^{\mathrm{int}} = \int_{\Gamma_{\mathrm{b}}} \left(\delta\boldsymbol{\lambda}_{\mathrm{f}} \cdot \left\{\mathbf{B}^{\mathsf{T}}(\mathbf{x}_{\mathrm{f}} - \mathbf{x}_b)\right\} + (\delta\mathbf{u}_{\mathrm{f}} - \delta\mathbf{u}_b) \cdot \{\mathbf{B}\boldsymbol{\lambda}_{\mathrm{f}}\}\right) \mathrm{d}A, \tag{50}$$

$$\delta\pi_{\mathrm{s}}^{\mathrm{int}} = \int_{\Gamma_{\mathrm{b}}} \left(\delta\boldsymbol{\lambda}_{\mathrm{s}} \cdot \left\{\mathbf{B}^{\mathsf{T}}(\mathbf{x}_{\mathrm{s}} - \mathbf{x}_b)\right\} + (\delta\mathbf{u}_{\mathrm{s}} - \delta\mathbf{u}_b) \cdot \{\mathbf{B}\boldsymbol{\lambda}_{\mathrm{s}}\}\right) \mathrm{d}A. \tag{51}$$

Collecting contributions (44), the final expression for the interface functional variation is

$$\begin{aligned}\delta\pi^{\mathrm{f}}(\mathbf{x}_{\mathrm{f}}, \mathbf{x}_{\mathrm{s}}, \boldsymbol{\lambda}_{\mathrm{f}}, \boldsymbol{\lambda}_{\mathrm{s}}, \mathbf{x}_b) = &\int_{\Gamma_b} \delta\mathbf{u}_{\mathrm{f}} \cdot \{\mathbf{B}\boldsymbol{\lambda}_{\mathrm{f}}\} \mathrm{d}A + \int_{\Gamma_b} \delta\mathbf{u}_{\mathrm{s}} \cdot \{\mathbf{B}\boldsymbol{\lambda}_{\mathrm{s}}\} \mathrm{d}A \\ &+ \int_{\Gamma_b} \delta\boldsymbol{\lambda}_{\mathrm{f}} \cdot \left\{\mathbf{B}^{\mathsf{T}}(\mathbf{x}_{\mathrm{f}} - \mathbf{x}_b)\right\} \mathrm{d}A + \int_{\Gamma_b} \delta\boldsymbol{\lambda}_{\mathrm{s}} \cdot \left\{\mathbf{B}^{\mathsf{T}}(\mathbf{x}_{\mathrm{s}} - \mathbf{x}_b)\right\} \mathrm{d}A \\ &- \int_{\Gamma_b} \delta\mathbf{u}_b \cdot \{\mathbf{B}(\boldsymbol{\lambda}_{\mathrm{f}} + \boldsymbol{\lambda}_{\mathrm{s}})\} \mathrm{d}A.\end{aligned} \tag{52}$$

Here, independently varied fields are listed in parenthesis on the left-hand side. Note that in equation (52), the following terms can be identified from the fluid side

$$G_{u_{\mathrm{f}}}(\boldsymbol{\lambda}_{\mathrm{f}}; \delta\mathbf{u}_{\mathrm{f}}) = \int_{\Gamma_{\mathrm{b}}} \delta\mathbf{u}_{\mathrm{f}} \cdot \{\mathbf{B}\boldsymbol{\lambda}_{\mathrm{f}}\} \mathrm{d}A, \tag{53}$$

$$G_{\lambda_{\mathrm{f}}}(\mathbf{x}_{\mathrm{f}}, \mathbf{x}_b; \delta\boldsymbol{\lambda}_{\mathrm{f}}) = \int_{\Gamma_{\mathrm{b}}} \left(\delta\boldsymbol{\lambda}_{\mathrm{f}} \cdot \left\{\mathbf{B}^{\mathsf{T}}(\mathbf{X}_{\mathrm{f}} - \mathbf{x}_b)\right\}\right) \mathrm{d}A, \tag{54}$$

$$G_{u_b}(\boldsymbol{\lambda}_{\mathrm{f}}; \delta\mathbf{u}_b) = -\int_{\Gamma_{\mathrm{b}}} \delta\mathbf{u}_b \cdot \{\mathbf{B}\boldsymbol{\lambda}_{\mathrm{f}}\} \mathrm{d}A, \tag{55}$$

with similar expressions for the structure side. Here, $G_{u_{\mathrm{f}}}(\boldsymbol{\lambda}_{\mathrm{f}}; \delta\mathbf{u}_{\mathrm{f}})$ represents the virtual work of interface forces acting on the fluid, $G_{\lambda_{\mathrm{f}}}(\mathbf{x}_{\mathrm{f}}, \mathbf{x}_b; \delta\boldsymbol{\lambda}_{\mathrm{f}})$ is the kinematic constraint between the fluid and the frame, whereas $G_{u_b}(\boldsymbol{\lambda}_{\mathrm{f}}; \delta\mathbf{u}_b)$ is the virtual work carried out by the interface forces on the

DOI: 10.1002/nme

frame. Combining these terms with their counterparts from the structure, the final force equilibrium conditions to be satisfied on the frame can be compactly stated as

$$G_{u_b}(\boldsymbol{\lambda}_\mathrm{f};\delta\mathbf{u}_b)+G_{u_b}(\boldsymbol{\lambda}_\mathrm{s};\delta\mathbf{u}_b)=0 \tag{56}$$

If the fluid model is inviscid, FSI takes place only in the normal direction to the wet surface $\mathbf{n}$, which is conventionally selected to be exterior to the fluid. In this case, the localized Lagrangian multipliers $(\lambda_\mathrm{f},\lambda_\mathrm{s})$ and the frame displacements (u_b) need to carry only the normal component, and the interface functional reduces to

$$\begin{aligned}\delta\pi^\mathrm{f}(\mathbf{x}_\mathrm{f},\mathbf{x}_\mathrm{s},\lambda_\mathrm{f},\lambda_\mathrm{s},x_b)=&\int_{\Gamma_b}\delta\mathbf{u}_\mathrm{f}\cdot\{\lambda_\mathrm{f}\mathbf{n}\}\,\mathrm{d}A+\int_{\Gamma_b}\delta\mathbf{u}_\mathrm{s}\cdot\{\lambda_\mathrm{s}\mathbf{n}\}\,\mathrm{d}A\\&+\int_{\Gamma_b}\delta\lambda_\mathrm{f}(\mathbf{x}_\mathrm{f}\cdot\mathbf{n}-x_b)\,\mathrm{d}A+\int_{\Gamma_b}\delta\lambda_\mathrm{s}(\mathbf{x}_\mathrm{s}\cdot\mathbf{n}-x_b)\,\mathrm{d}A\\&-\int_{\Gamma_b}(\lambda_\mathrm{f}+\lambda_\mathrm{s})\delta u_b\,\mathrm{d}A.\end{aligned} \tag{57}$$

Here, λ_f and λ_s are LLM functions in the normal direction that link the independently varied normal displacement function of the frame u_b with the displacement fields of the fluid $\mathbf{u}_\mathrm{f}$ and the structure $\mathbf{u}_\mathrm{s}$. Finally, it is important to mention that the preceding interface constraint functional is a linear approximation that is valid for small variations of local system $\mathbf{B}$. For a complete nonlinear formulation of the moving frame, the reader is referred to [59–61].

7.2. Discretization of interface constraint functional

To construct discrete matrix forms of the interface equations, functional (57) is discretized by assuming shape functions for the independently varied fields: λ_f, λ_s, and u_b. The approximation for boundary displacements $\mathbf{u}_\mathrm{f}$ and $\mathbf{u}_\mathrm{s}$ comes from the finite elements used for the fluid and structure models, respectively, and are expressed in the global reference system. The normal displacements $\mathbf{u}_b(\xi_1,\xi_2)$ of the interface frame are interpolated using isoparametric finite elements in the conventional form

$$\mathbf{u}_b(\xi_1,\xi_2)=\mathbf{N}_b(\xi_1,\xi_2)\left\{\begin{array}{c}u_{b_1}\\ \vdots\\ u_{b_{n_b}}\end{array}\right\}=N_{bi}(\boldsymbol{\xi})u_{bi}. \tag{58}$$

Here, $\boldsymbol{\xi}=(\xi_1,\xi_2)$ are natural frame coordinates, and n_b is the number of nodes in the frame element. The shape functions for $\mathbf{N}_b$ will be piecewise linear, C^0-continuous [62–66].

If the normal multipliers are discretized as $\lambda_\mathrm{f}=\mathbf{N}_{\lambda_\mathrm{f}}\boldsymbol{\lambda}_\mathrm{f}$, $\lambda_\mathrm{s}=\mathbf{N}_{\lambda_\mathrm{s}}\boldsymbol{\lambda}_\mathrm{s}$, then insertion of these interpolations in $\delta\pi^\mathrm{f}$ and integration over Γ_b produce the discrete interface functional as

$$\begin{aligned}\delta\pi^\mathrm{f}=&\delta\mathbf{u}_\mathrm{f}^\mathsf{T}\mathbf{B}_\mathrm{f}\mathbf{u}_\mathrm{f}+\delta\mathbf{u}_\mathrm{s}^\mathsf{T}\mathbf{B}_\mathrm{s}\mathbf{u}_\mathrm{s}+\delta\boldsymbol{\lambda}_\mathrm{f}^\mathsf{T}\left(\mathbf{B}_\mathrm{f}^\mathsf{T}\mathbf{x}_\mathrm{f}-\mathbf{L}_\mathrm{f}\mathbf{x}_b\right)\\&+\delta\boldsymbol{\lambda}_\mathrm{s}^\mathsf{T}\left(\mathbf{B}_\mathrm{s}^\mathsf{T}\mathbf{x}_\mathrm{s}-\mathbf{L}_\mathrm{s}\mathbf{x}_b\right)-\delta\mathbf{u}_b^\mathsf{T}\left(\mathbf{L}_\mathrm{f}^\mathsf{T}\boldsymbol{\lambda}_\mathrm{f}+\mathbf{L}_\mathrm{s}^\mathsf{T}\boldsymbol{\lambda}_\mathrm{s}\right),\end{aligned} \tag{59}$$

in which

$$\mathbf{B}_\mathrm{f}=\int_{\Gamma_b}\mathbf{N}_\mathrm{f}^\mathsf{T}\mathbf{n}\mathbf{N}_{\lambda_\mathrm{f}}\,\mathrm{d}A \tag{60}$$

$$\mathbf{B}_\mathrm{s}=\int_{\Gamma_b}\mathbf{N}_\mathrm{s}^\mathsf{T}\mathbf{n}\mathbf{N}_{\lambda_\mathrm{s}}\,\mathrm{d}A \tag{61}$$

$$\mathbf{L}_\mathrm{f}=\int_{\Gamma_b}\mathbf{N}_{\lambda_\mathrm{f}}^\mathsf{T}\mathbf{N}_b\,\mathrm{d}A \tag{62}$$

DOI: 10.1002/nme

$$\mathbf{L}_{\mathrm{s}} = \int_{\Gamma_b} \mathbf{N}_{\lambda_{\mathrm{s}}}^{\mathrm{T}} \mathbf{N}_b \, \mathrm{d}A \tag{63}$$

Here, $\mathbf{N}_{\mathrm{f}}$ and $\mathbf{N}_{\mathrm{s}}$ denote the shape functions of the fluid and structure displacement elements, respectively, evaluated on the discretized interface surface Γ_b. In some cases, as in curved geometries, the discretized interface may differ slightly from the original one [35].

The integral evaluations in (60)–(63) are greatly simplified by assuming that $\mathbf{N}_{\lambda_{\mathrm{f}}}$ and $\mathbf{N}_{\lambda_{\mathrm{s}}}$ are Dirac delta functions collocated at the fluid and structure interface nodes, respectively. If so, $\mathbf{B}_{\mathrm{f}}$ and $\mathbf{B}_{\mathrm{s}}$ become Boolean matrices that select and normal-project node boundary freedoms from the complete state vectors $\mathbf{u}_{\mathrm{f}}$ and $\mathbf{u}_{\mathrm{s}}$, whereas $\mathbf{L}_{\mathrm{f}}$ and $\mathbf{L}_{\mathrm{s}}$ simply become the evaluation on the frame of boundary node positions.

Our choice for multiplier discretization, as illustrated in Figure 5, is to model them as concentrated forces, that is, the multiplier support functions are *Dirac* delta functions

$$\lambda_{\mathrm{f}}(\boldsymbol{\xi}) = N_{\lambda_{\mathrm{f}} i}(\boldsymbol{\xi}) \lambda_{\mathrm{f}i} \; ; \; N_{\lambda_{\mathrm{f}} i}(\boldsymbol{\xi}) = \delta(\boldsymbol{\xi} - \boldsymbol{\xi}_p) \tag{64}$$

$$\lambda_{\mathrm{s}}(\boldsymbol{\xi}) = N_{\lambda_{\mathrm{s}} i}(\boldsymbol{\xi}) \lambda_{\mathrm{s}i} \; ; \; N_{\lambda_{\mathrm{s}} i}(\boldsymbol{\xi}) = \delta(\boldsymbol{\xi} - \boldsymbol{\xi}_p) \tag{65}$$

where $\boldsymbol{\xi}_p$ is the frame coordinate of the fluid or structural interface node projected on the frame. If the interface is defined in terms of *pairs* or couples, formed by an interface node and its projection on the frame, then the integration of the multiplier field over the contact zone is reduced to summations over pairs, that is,

$$\int_{\Gamma_{\mathrm{b}}} \boldsymbol{\lambda}_{\mathrm{f}}(\boldsymbol{\xi}) \cdot \mathbf{f}(\boldsymbol{\xi}) \, d\Gamma_{\mathrm{b}} = \sum_{p=1}^{n_p} \boldsymbol{\lambda}_{\mathrm{f}}^{(p)} \cdot \mathbf{f}(\boldsymbol{\xi}_p), \tag{66}$$

in which $\mathbf{f}(\boldsymbol{\xi})$ is a general function and n_p the total number of pairs on the fluid side. Expression (66) is the key in order to maintain the interface treatment generic, leading to modular coupling software because the frame needs to know very little information about the system it is interfacing.

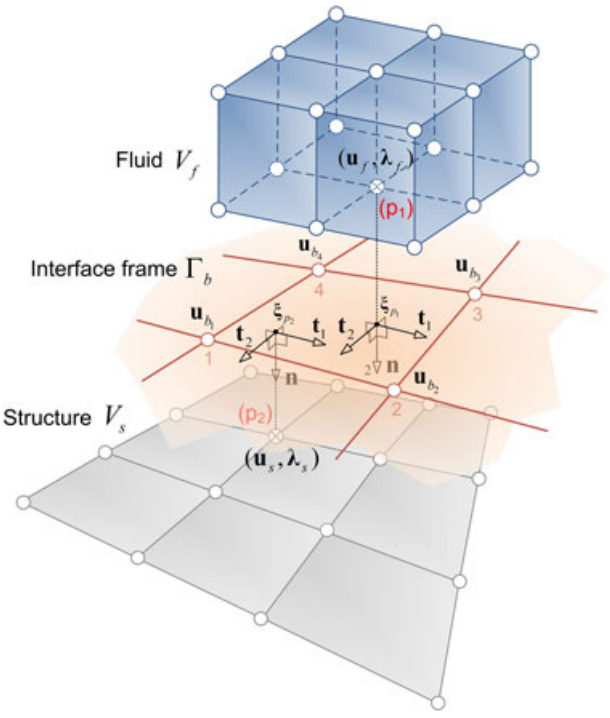

Figure 5. Exploded view of the fluid–structure interface discretization. Interface nodes of the fluid and the structure are projected on the frame constituting *pairs* or couples formed by the hitting node and its closest frame element.

DOI: 10.1002/nme

To manage the discrete variables, we have to introduce the interface nodal indicator $\mathcal{B}$, the Boolean finite element assembling operator defined in the following way

$$\mathbf{u}_{\mathrm{f}}^{(p)} = \mathcal{B}_{u_{\mathrm{f}}}^{(p)} \mathbf{u}_{\mathrm{f}} \tag{67}$$

$$\mathbf{u}_{\mathrm{s}}^{(p)} = \mathcal{B}_{u_{\mathrm{s}}}^{(p)} \mathbf{u}_{\mathrm{s}} \tag{68}$$

$$\mathbf{u}_{b}^{(p)} = \mathcal{B}_{u_{b}}^{(p)} \mathbf{u}_{b} \tag{69}$$

and

$$\boldsymbol{\lambda}_{\mathrm{f}}^{(p)} = \mathcal{B}_{\lambda_{\mathrm{f}}}^{(p)} \boldsymbol{\lambda}_{\mathrm{f}} \tag{70}$$

$$\boldsymbol{\lambda}_{\mathrm{s}}^{(p)} = \mathcal{B}_{\lambda_{\mathrm{s}}}^{(p)} \boldsymbol{\lambda}_{\mathrm{s}} \tag{71}$$

where $\mathcal{B}_{\square}^{(p)}$ is used to extract the variable associated with a boundary node (p) from the global vector of $\square$ unknowns with $\square = u_{\mathrm{f}}, u_{\mathrm{s}}, \lambda_{\mathrm{f}}, \lambda_{\mathrm{s}}, u_b$. By using this operator together with (66), matrices (60)–(63) are simply obtained assembling contributions of each pair (p) in the following way

$$\mathbf{B}_{\mathrm{f}} = \sum_{p=1}^{n_p} \mathcal{B}_{u_{\mathrm{f}}}^{(p)\mathsf{T}} \mathbf{n}(\boldsymbol{\xi}_p) \mathcal{B}_{\lambda_{\mathrm{f}}}^{(p)} \tag{72}$$

$$\mathbf{B}_{\mathrm{s}} = \sum_{p=1}^{n_p} \mathcal{B}_{u_{\mathrm{s}}}^{(p)\mathsf{T}} \mathbf{n}(\boldsymbol{\xi}_p) \mathcal{B}_{\lambda_{\mathrm{s}}}^{(p)} \tag{73}$$

$$\mathbf{L}_{\mathrm{f}} = \sum_{p=1}^{n_p} \mathcal{B}_{\lambda_{\mathrm{f}}}^{(p)\mathsf{T}} \mathbf{N}_b(\boldsymbol{\xi}_p) \mathcal{B}_{u_b}^{(p)} \tag{74}$$

$$\mathbf{L}_{\mathrm{s}} = \sum_{p=1}^{n_p} \mathcal{B}_{\lambda_{\mathrm{s}}}^{(p)\mathsf{T}} \mathbf{N}_b(\boldsymbol{\xi}_p) \mathcal{B}_{u_b}^{(p)} \tag{75}$$

with sums extended to the n_p active pairs of the corresponding side: fluid or structure.

8. FRAME CONSTRUCTION

The interface formulation presented so far relies on the assumption that there exists a discretization for the frame representing the fluid–structure interface. But the problem of defining a mesh for the interface frame is not unique if the fluid and structure meshes are non-matching [65]. For example, one could construct a frame mesh coincident with the structure discretization at the interface, or with the fluid discretization, or to define a different mesh between those two. However, these arbitrary choices in general will not satisfy the force patch test through the interface [67, 68].

For constructing an interface mesh that satisfies the requirement of unicity and passes the force patch test, the node locations of the interface frame are decided using the Zero-Moment Rule (ZMR) originally proposed for contact–impact problems [61]. The main concept behind the ZMR is to assure that the LLMs can exactly transmit a constant-stress state through the interface frame, thus passing the patch test. This condition can be satisfied if the interface node locations are determined by the roots of the frame moment–equilibrium condition [62, 66].

The frame construction process is schematized in Figure 6, in which nodal positions of the fluid interface $\mathbf{x}_{\mathrm{f}}$ and the structure interface $\mathbf{x}_{\mathrm{s}}$ are considered known and a bending moment diagram $\mathcal{M}(\mathbf{x})$, due to the nodal forces corresponding to a constant-stress state, is constructed. The ZMR

DOI: 10.1002/nme

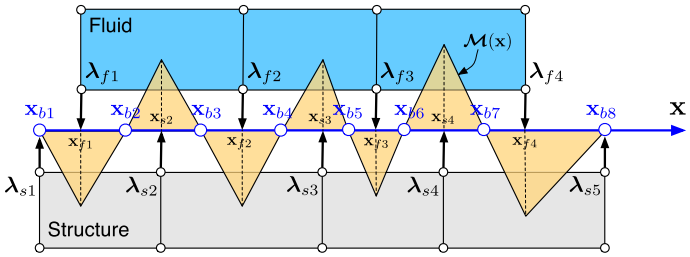

Figure 6. Frame construction using a defined position of the fluid $\mathbf{x}_{\mathrm{f}}$ and the structure $\mathbf{x}_{\mathrm{s}}$. Frame nodes are located at $\mathbf{x}_b$, zero-moment roots of the bending moment diagram $\mathcal{M}(\mathbf{x})$ produced by the forces acting on the frame.

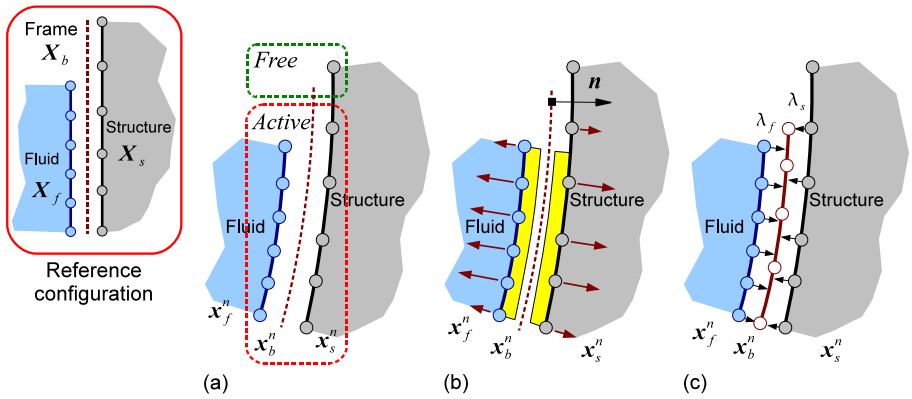

Figure 7. Steps in the definition of the frame based on position $\mathbf{x}_b^n$: (a) detection of active interface nodes, (b) computation of nodal forces corresponding to a constant pressure transmission, and (c) construction of a new frame discretization using the ZMR. Separation between fluid and structure is exaggerated for better visualization.

states that, for preservation of constant-stress states, the location of the frame nodes $\mathbf{x}_b$ must coincide with the roots of $\mathcal{M}(\mathbf{x})$. This rule can be expressed as

$$\mathbf{x}_b = \mathcal{M}_0(\mathbf{x}_{\mathrm{f}}, \mathbf{x}_{\mathrm{s}}) \tag{76}$$

where $\mathcal{M}_0$ represents the roots of the bending moment function for a certain position of the fluid and the structure.

For a viscous fluid, imposing the kinematic condition (42) fixes the relative position of fluid and structure meshes at the interface; therefore, the interface-frame mesh is constant. However, an inviscid fluid requires free relative tangential motion between the fluid and structure interface meshes, as dictated by condition (43). This condition makes the position of the fluid and structure interface nodes on the frame time dependent. This situation requires the frame mesh to be recalculated every time step by using a similar procedure to that employed in contact–impact problems [66].

Let us suppose that we have arrived to time step t^n and we know the total positions of the fluid $\left(\mathbf{x}_{\mathrm{f}}^n\right)$, frame $\left(\mathbf{x}_b^n\right)$, and structure $\left(\mathbf{x}_{\mathrm{s}}^n\right)$. The procedure used to construct a frame satisfying the ZMR for time step t^{n+1} is graphically explained in Figure 7 and can be summarized in the following steps:

1. Define the active boundary for t^{n+1}. Search for active interface nodes based on the total position of the fluid $\mathbf{x}_{\mathrm{f}}^n$ relative to the position of the structure $\mathbf{x}_{\mathrm{s}}^n$. Find free nodes and disconnect them from the interface region.
2. Suppose the transmission of a constant normal stress through the active boundary. Compute the contribution of every interface element to that constant stress by evaluating its equivalent nodal forces.

DOI: 10.1002/nme

3. Using previous nodal forces together with their total position $\left(\mathbf{x}_{\mathrm{f}}^{n}, \mathbf{x}_{\mathrm{s}}^{n}\right)$, apply the ZMR to obtain the location of the new frame nodes $\mathbf{x}_{b}^{n} = \boldsymbol{\mathcal{M}}_0\left(\mathbf{x}_{\mathrm{f}}^{n}, \mathbf{x}_{\mathrm{s}}^{n}\right)$.
4. Construct a frame mesh with isoparametric elements by using the previous frame nodes.
5. Project the current position of the fluid and the structure active nodes on the frame elements forming a new group of pairs. For each pair, calculate the position $\boldsymbol{\xi}_p$ of the interface node in the frame element, the normal in that position $\mathbf{n}(\boldsymbol{\xi}_p)$, and shape functions $\mathbf{N}_b(\boldsymbol{\xi}_p)$.

Once the frame is defined, the FSI problem is solved for time step t^{n+1}, obtaining new positions $\mathbf{x}_{\mathrm{f}}^{n+1}$ and $\mathbf{x}_{\mathrm{s}}^{n+1}$. The frame definition algorithm can then be repeated for a new time step.

9. PARTITIONED FLUID–STRUCTURE FORMULATION

The partitioned FSI model can now be constructed following the variational statement given in (2) for the discrete form of the total energy functional variation $\delta\Pi$. Inserting the discrete variational internal constraint (59), the discrete variational fluid equation (37) and the discrete variational structural equation (40) into the foregoing equation gives the variational form

$$\begin{aligned}\delta\Pi = {} & \delta\mathbf{u}_{\mathrm{f}}^{\mathsf{T}}\left\{\mathbf{M}_{\mathrm{f}}\ddot{\mathbf{u}}_{\mathrm{f}} + \mathbf{K}_{\mathrm{f}}\mathbf{u}_{\mathrm{f}} + \mathbf{B}_{\mathrm{f}}\boldsymbol{\lambda}_{\mathrm{f}} - \mathbf{f}_{\mathrm{f}}\right\} \\ & + \delta\mathbf{u}_{\mathrm{s}}^{\mathsf{T}}\left\{\mathbf{M}_{\mathrm{s}}\ddot{\mathbf{u}}_{\mathrm{s}} + \mathbf{K}_{\mathrm{s}}\mathbf{u}_{\mathrm{s}} + \mathbf{B}_{\mathrm{s}}\boldsymbol{\lambda}_{\mathrm{s}} - \mathbf{f}_{\mathrm{s}}\right\} \\ & + \delta\boldsymbol{\lambda}_{\mathrm{f}}^{\mathsf{T}}\left\{\mathbf{B}_{\mathrm{f}}^{\mathsf{T}}\mathbf{u}_{\mathrm{f}} - \mathbf{L}_{\mathrm{f}}\mathbf{u}_{b} - \mathbf{h}_{\mathrm{f}}\right\} + \delta\boldsymbol{\lambda}_{\mathrm{s}}^{\mathsf{T}}\left\{\mathbf{B}_{\mathrm{s}}^{\mathsf{T}}\mathbf{u}_{\mathrm{s}} - \mathbf{L}_{\mathrm{s}}\mathbf{u}_{b} - \mathbf{h}_{\mathrm{s}}\right\} \\ & - \delta\mathbf{u}_{b}^{\mathsf{T}}\left\{\mathbf{L}_{\mathrm{f}}^{\mathsf{T}}\boldsymbol{\lambda}_{\mathrm{f}} + \mathbf{L}_{\mathrm{s}}^{\mathsf{T}}\boldsymbol{\lambda}_{\mathrm{s}}\right\}\end{aligned} \tag{77}$$

in which vectors $\mathbf{h}_{\mathrm{f}} = \left(\mathbf{B}_{\mathrm{f}}^{\mathsf{T}}\mathbf{X}_{\mathrm{f}} - \mathbf{L}_{\mathrm{f}}\mathbf{X}_{b}\right)$ and $\mathbf{h}_{\mathrm{s}} = \left(\mathbf{B}_{\mathrm{s}}^{\mathsf{T}}\mathbf{X}_{\mathrm{s}} - \mathbf{L}_{\mathrm{s}}\mathbf{X}_{b}\right)$ are function of the initial configuration. Making (77) stationary with respect to the primary vaariables yields the partitioned, semidiscrete equations of motion

$$\begin{bmatrix} \mathbf{K}_{\mathrm{f}} + \mathbf{M}_{\mathrm{f}}\frac{\mathrm{d}^2}{\mathrm{d}t^2} & \mathbf{0} & \mathbf{B}_{\mathrm{f}} & \mathbf{0} & \mathbf{0} \\ \mathbf{0} & \mathbf{K}_{\mathrm{s}} + \mathbf{M}_{\mathrm{s}}\frac{\mathrm{d}^2}{\mathrm{d}t^2} & \mathbf{0} & \mathbf{B}_{\mathrm{s}} & \mathbf{0} \\ \mathbf{B}_{\mathrm{f}}^{\mathsf{T}} & \mathbf{0} & \mathbf{0} & \mathbf{0} & -\mathbf{L}_{\mathrm{f}} \\ \mathbf{0} & \mathbf{B}_{\mathrm{s}}^{\mathsf{T}} & \mathbf{0} & \mathbf{0} & -\mathbf{L}_{\mathrm{s}} \\ \mathbf{0} & \mathbf{0} & -\mathbf{L}_{\mathrm{f}}^{\mathsf{T}} & -\mathbf{L}_{\mathrm{s}}^{\mathsf{T}} & \mathbf{0} \end{bmatrix} \begin{Bmatrix} \mathbf{u}_{\mathrm{f}} \\ \mathbf{u}_{\mathrm{s}} \\ \boldsymbol{\lambda}_{\mathrm{f}} \\ \boldsymbol{\lambda}_{\mathrm{s}} \\ \mathbf{u}_{b} \end{Bmatrix} = \begin{Bmatrix} \mathbf{f}_{\mathrm{f}} \\ \mathbf{f}_{\mathrm{s}} \\ \mathbf{h}_{\mathrm{f}} \\ \mathbf{h}_{\mathrm{s}} \\ \mathbf{0} \end{Bmatrix}. \tag{78}$$

The first two rows of the foregoing matrix equation are the discrete equilibrium equations and the fluid and structure partitions, respectively, with terms $\mathbf{B}_{\mathrm{f}}\boldsymbol{\lambda}_{\mathrm{f}}$ and $\mathbf{B}_{\mathrm{s}}\boldsymbol{\lambda}_{\mathrm{s}}$ representing the interaction forces transacted through the frame. The third and fourth equations impose fluid–frame and structure–frame displacement compatibility, respectively. The last equation states the equilibrium of the frame.

9.1. Vibration analysis

The equation of motion (78) can be specialized to small, unforced oscillations of frequency ω about an equilibrium configuration by replacing the time-differentiation operator $\frac{\mathrm{d}^2}{\mathrm{d}t^2}$ with $-\omega^2$ and setting external forces to zero:

$$\begin{bmatrix} \mathbf{K}_{\mathrm{f}} - \omega^2\mathbf{M}_{\mathrm{f}} & \mathbf{0} & \mathbf{B}_{\mathrm{f}} & \mathbf{0} & \mathbf{0} \\ \mathbf{0} & \mathbf{K}_{\mathrm{s}} - \omega^2\mathbf{M}_{\mathrm{s}} & \mathbf{0} & \mathbf{B}_{\mathrm{s}} & \mathbf{0} \\ \mathbf{B}_{\mathrm{f}}^{\mathsf{T}} & \mathbf{0} & \mathbf{0} & \mathbf{0} & -\mathbf{L}_{\mathrm{f}} \\ \mathbf{0} & \mathbf{B}_{\mathrm{s}}^{\mathsf{T}} & \mathbf{0} & \mathbf{0} & -\mathbf{L}_{\mathrm{s}} \\ \mathbf{0} & \mathbf{0} & -\mathbf{L}_{\mathrm{f}}^{\mathsf{T}} & -\mathbf{L}_{\mathrm{s}}^{\mathsf{T}} & \mathbf{0} \end{bmatrix} \begin{Bmatrix} \mathbf{u}_{\mathrm{f}} \\ \mathbf{u}_{\mathrm{s}} \\ \boldsymbol{\lambda}_{\mathrm{f}} \\ \boldsymbol{\lambda}_{\mathrm{s}} \\ \mathbf{u}_{b} \end{Bmatrix} = \begin{Bmatrix} \mathbf{0} \\ \mathbf{0} \\ \mathbf{0} \\ \mathbf{0} \\ \mathbf{0} \end{Bmatrix}. \tag{79}$$

This is a generalized, symmetric, algebraic eigenvalue problem from which frequencies and mode shapes of the coupled system can be determined [34].

DOI: 10.1002/nme

9.2. Transient response analysis

The semidiscrete equations of motion (78) may be directly integrated in time to obtained the transient response of the coupled system. By using Newmark's method as time integrator, the displacements, velocities, and accelerations at the next time step t^{n+1} are related to quantities of the previous time step t^n by

$$\mathbf{u}^{n+1} = \mathbf{u}^n + \Delta t \dot{\mathbf{u}}^n + \Delta t^2 \left[\left(\frac{1}{2} - \beta \right) \ddot{\mathbf{u}}^n + \beta \ddot{\mathbf{u}}^{n+1} \right], \tag{80}$$

$$\dot{\mathbf{u}}^{n+1} = \dot{\mathbf{u}}^n + \Delta t \left[(1-\gamma) \ddot{\mathbf{u}}^n + \gamma \ddot{\mathbf{u}}^{n+1} \right]. \tag{81}$$

Here, $\Delta t = t^{n+1} - t^n$ is the time step, whereas (β, γ) are method parameters that control stability and accuracy characteristics. In the numerical examples reported here, both parameters are taken to be the same for both fluid ($\mathbf{u} = \mathbf{u}_\mathrm{f}$) and structure ($\mathbf{u} = \mathbf{u}_\mathrm{s}$). Suppose now that computations have proceeded until t^n. Inserting (80) and (81) into the matrix equation (78) and passing all information from the previous time step to the right-hand side yield

$$\begin{bmatrix} \mathbf{M}_\mathrm{f} + \beta \Delta t^2 \mathbf{K}_\mathrm{f} & \mathbf{0} & \mathbf{B}_\mathrm{f} & \mathbf{0} & \mathbf{0} \\ \mathbf{0} & \mathbf{K}_\mathrm{s} + \beta \Delta t^2 \mathbf{M}_\mathrm{s} & \mathbf{0} & \mathbf{B}_\mathrm{s} & \mathbf{0} \\ \mathbf{B}_\mathrm{f}^\mathsf{T} & \mathbf{0} & \mathbf{0} & \mathbf{0} & -\mathbf{L}_\mathrm{f} \\ \mathbf{0} & \mathbf{B}_\mathrm{s}^\mathsf{T} & \mathbf{0} & \mathbf{0} & -\mathbf{L}_\mathrm{s} \\ \mathbf{0} & \mathbf{0} & -\mathbf{L}_\mathrm{f}^\mathsf{T} & -\mathbf{L}_\mathrm{s}^\mathsf{T} & \mathbf{0} \end{bmatrix} \begin{Bmatrix} \ddot{\mathbf{u}}_\mathrm{f} \\ \ddot{\mathbf{u}}_\mathrm{s} \\ \boldsymbol{\lambda}_\mathrm{f} \\ \boldsymbol{\lambda}_\mathrm{s} \\ \ddot{\mathbf{u}}_b \end{Bmatrix}^{n+1} = \begin{Bmatrix} \mathbf{g}_\mathrm{f} \\ \mathbf{g}_\mathrm{s} \\ \mathbf{h}_\mathrm{f} \\ \mathbf{h}_\mathrm{s} \\ \mathbf{0} \end{Bmatrix}^{n+1}, \tag{82}$$

in which

$$\mathbf{g}_\mathrm{f}^{n+1} = \mathbf{f}_\mathrm{f}^{n+1} - \mathbf{K}_\mathrm{f} \left[\mathbf{u}_\mathrm{f}^n + \Delta t \dot{\mathbf{u}}_\mathrm{f}^n + \Delta t^2 \left(\frac{1}{2} - \beta \right) \ddot{\mathbf{u}}_\mathrm{f}^n \right] \tag{83}$$

$$\mathbf{g}_\mathrm{s}^{n+1} = \mathbf{f}_\mathrm{s}^{n+1} - \mathbf{K}_\mathrm{s} \left\{ \mathbf{u}_\mathrm{s}^n + \Delta t \dot{\mathbf{u}}_\mathrm{s}^n + \Delta t^2 \left(\frac{1}{2} - \beta \right) \ddot{\mathbf{u}}_\mathrm{s}^n \right\} \tag{84}$$

It has been demonstrated by Ross *et al.* [64] that in partitioned FSI problems treated with localized Lagrangian multipliers, as well as with mortar and monolithic treatments, Newmark's method with $\left(\beta = \frac{1}{4}, \gamma = \frac{1}{2}\right)$ provides A-stability and global second-order accuracy. This selection of parameters, which is equivalent to the well-known Trapezoidal Rule, is used for time integration in all our numerical applications.

10. APPLICATION EXAMPLES

The following application examples serve to verify and illustrate the capabilities of the proposed formulation in the modeling and simulation of FSI problems. Examples are selected to demonstrate the proper capturing of three different physical effects considered in the fluid component: initial hydrostatic state, sloshing, and acoustic waves, together with strong FSI effects. To model the fluid, isoparametric quadrilateral elements are used in 2D and isoparametric eight-node brick elements in 3D.

10.1. Two-dimensional acoustic cavity with a flexible wall

To isolate and study the contribution of the acoustic term in (32), we first consider a 2D problem consisting of a rectangular cavity of dimensions $L_x = 8$ m by $L_z = 20$ m with rigid walls, filled with water and closed on the top by a simply supported flexible beam (Figure 8).

The properties considered for the fluid (water) are $\rho_\mathrm{f} = 1000$ kg/m^3 and $c_\mathrm{f} = 1500$ m/s. The material properties of the structure are $E_\mathrm{s} = 210$ GPa and $\rho_\mathrm{s} = 2500$ kg/m^3, with a moment of inertia of the beam section $I_y = 1.59 \cdot 10^{-4}$ m^4.

DOI: 10.1002/nme

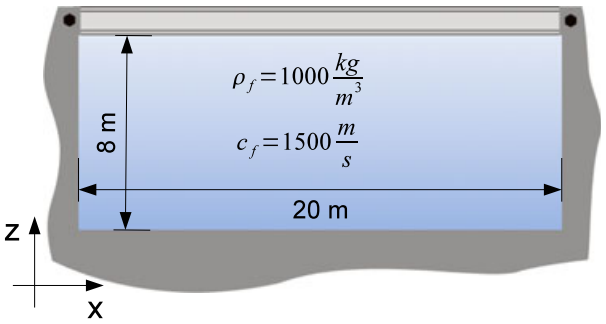

Figure 8. Sketch of a 2D cavity with three rigid walls closed by a flexible beam on the top.

Table I. Comparison of analytical and numerical acoustic frequencies obtained for a 2D acoustic cavity with rigid walls.

Acoustic freq.	Analytical (Hz)	Computed (Hz)
Mode (1,0)	37.5	37.5
Mode (0,1)	93.7	94.3
Mode (1,1)	100.9	101.3
Mode (2,1)	120.1	120.1
Mode (1,2)	191.2	195.6
Mode (2,2)	210.9	205.1

The fluid domain is meshed using 8×20 fluid elements, corresponding to 320 fluid DOFs. Each fluid element is square with a side length of 1 m. The structure on the top is modeled using 20 beam elements with two DOFs per node (vertical displacement and rotation) and connected to the fluid using localized Lagrangian multipliers.

The natural frequencies and structural modes that describe the dynamic behavior of the simply supported beam vibrating *in vacuo* are shown in Figure 10.

10.1.1. Case 1: Infinitely rigid beam. For later comparison with the flexible case, we first consider the limit $I_s \to \infty$, whence the top beam acts as another rigid wall, transforming the problem into an acoustic cavity with rigid walls. This limit problem has a well-known analytical solution. Resonance can be expected at frequencies for which the corresponding wavelengths match the dimensions of the cavity, that is,

$$\omega_{l,m}^2 = c_f k_{l,m} \qquad (l, m = 1, 2, 3, \ldots) \tag{85}$$

where $\omega_{l,m}$ is the resonant frequency and $k_{l,m} = \left(\left(\frac{l\pi}{L_x} \right)^2 + \left(\frac{m\pi}{L_z} \right)^2 \right)^{1/2}$ is the wave number.

Such frequencies are computed analytically using (85) and represented in Table I together with the numerical results obtained performing a vibration analysis using the technique described in Section 9.1. These first six resonant frequencies have been selected for contour plotting in Figure 9, with pictures showing horizontal and vertical displacements of the fluid, respectively, together with fluid pressure level that is constant inside each element as required by the mean dilatation method.

As expected, the approximation error of the acoustic modes in the horizontal direction is lower than in the vertical direction because of the coarser vertical discretization. For the displayed frequencies, the error is less than 3%. Observe that acoustic mode shapes for the selected frequencies are correctly captured.

10.1.2. Case 2: Flexible beam. Next, we study the effect of placing a flexible wall, with the dynamic characteristics summarized in Figure 10, on top of the cavity. The fundamental frequency

DOI: 10.1002/nme

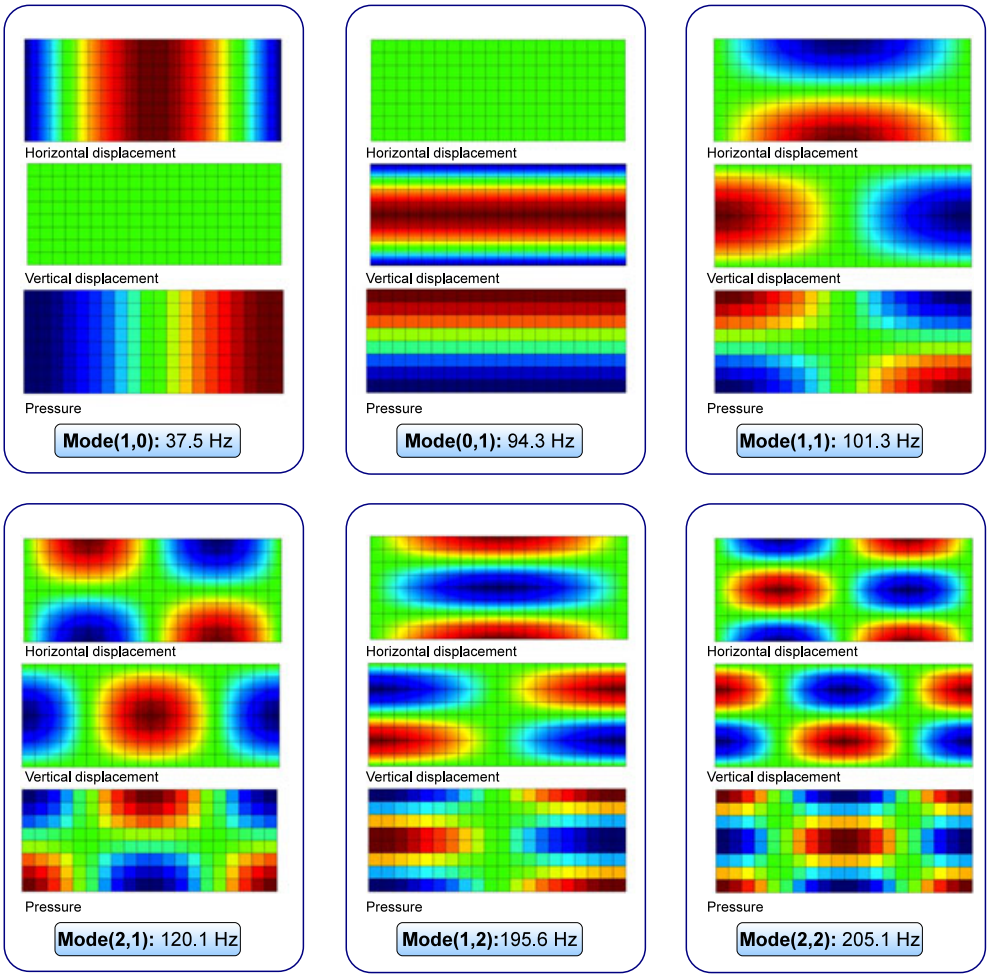

Figure 9. Results of vibration analysis for a 2D acoustic cavity with rigid walls. Acoustic modes for different frequencies.

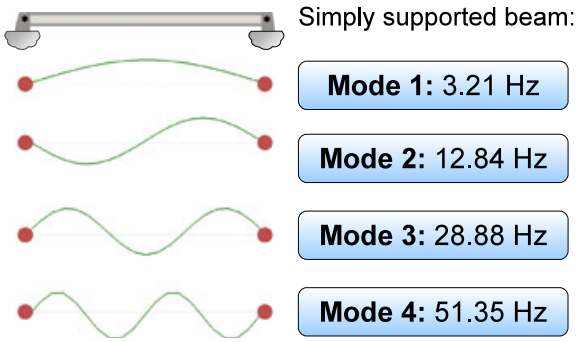

Figure 10. Structural natural frequencies of the beam vibrating *in vacuo* and associated mode shapes.

modes of the beam vibrating *in vacuo* involve more volumetric variation of the interior fluid, so frequencies are expected to vary significantly in the flexible case.

Figure 11 shows the first three vibration mode shapes of the rectangular cavity with elastic top boundary, along with associated frequencies. The mode shapes are greatly exaggerated and contour plots of the displacement fields are also represented. It is observed that the first three coupled modes

DOI: 10.1002/nme

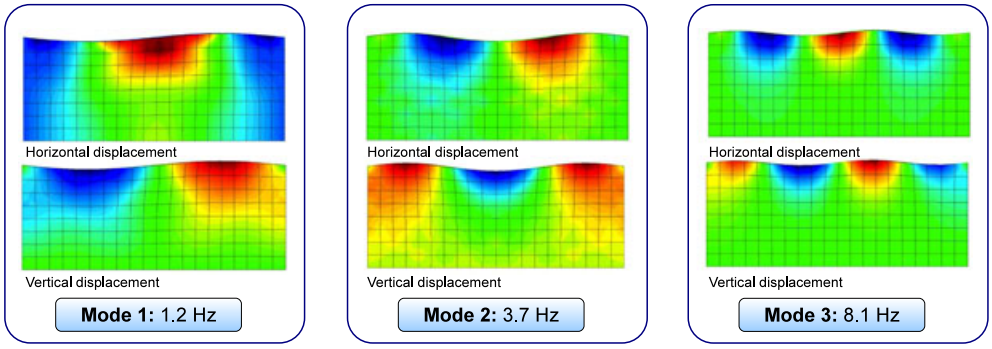

Figure 11. Coupled vibration modes obtained for a 2D acoustic cavity with flexible beam.

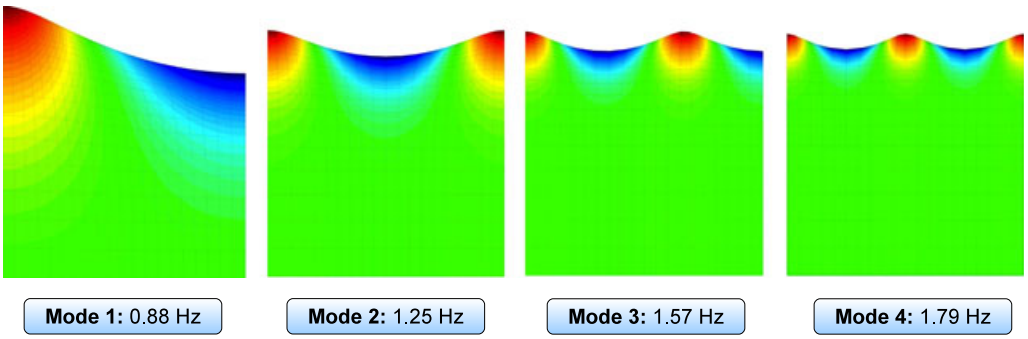

Figure 12. Sloshing modes with natural frequencies in a 2D container with rigid walls. The analytical solution of this case gives 0.88, 1.25, 1.53, and 1.77 Hz, for the first four modes.

are controlled by the flexible beam motion; however, the natural frequencies are lower due to added mass effects.

10.2. Sloshing in rigid containers

In this example, the fluid sloshing within a rigid container is studied for three different geometries: plane, cubic, and cylindrical. The fluid is water, with properties $\rho_{\mathrm{f}} = 1000\ \mathrm{kg/m^3}$ and $c_{\mathrm{f}} = 1500\ \mathrm{m/s}$. Sloshing frequencies and mode shapes can be computed from system (79), in which terms associated with the structure are discarded. An equivalent analysis procedure is used to solve for the transient response, in which case system (82) is directly integrated in time using Newmark's method.

10.2.1. Sloshing in rigid containers: vibration analysis. The first case considered is a 2D square container of width $B = 1$ m filled with water up to a height $H = 1$ m, and open to the atmosphere. The fluid volume is discretized using a regular mesh with 20×20 quadrilateral fluid elements and 441 nodes, as pictured in Figure 12, with mesh grading in the vertical direction. This refinement is introduced to better capture pressure gradient effects near the free surface.

Under the assumptions of incompressible inviscid fluid and irrotational flow, the exact analytical solution for this problem can be obtained by substituting the free-surface boundary condition into the velocity potential equation [1], which leads the classical solution for slosh frequencies

$$\omega_{l,m}^2 = g k_{l,m} \tanh(k_{l,m} H), \qquad (l, m = 1, 2, 3, \ldots) \tag{86}$$

in which g denotes the acceleration of gravity, $k_{l,m}$ the wavenumber and H the water depth. This analytical solution is compared with numerical results in Table II for the first four sloshing frequencies. Computed mode shapes corresponding to these frequencies are presented in Figure 12,

DOI: 10.1002/nme

Table II. Analytical/numerical comparison of the first four sloshing frequencies of a square container with rigid walls.

Sloshing freq.	Analytical (HZ)	Computed (HZ)
Mode 1	0.88	0.88
Mode 2	1.25	1.25
Mode 3	1.53	1.54
Mode 4	1.77	1.79

Table III. Analytical/numerical comparison of the first four sloshing frequencies of a cubic container with rigid walls.

Sloshing freq.	Analytical (Hz)	Computed (Hz)
Mode (1,0)	0.88	0.88
Mode (1,1)	1.05	1.04
Mode (2,0)	1.25	1.22
Mode (1,2)	1.32	1.28

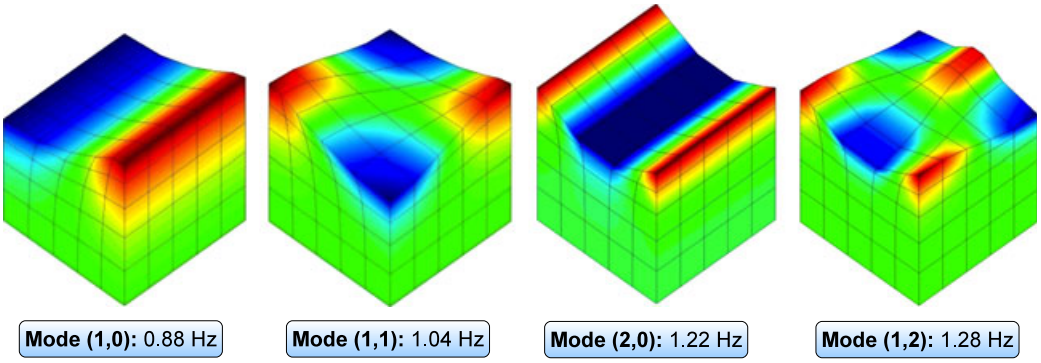

Figure 13. Sloshing modes and natural frequencies in a cubic container with rigid walls. The analytical solution of this case gives 0.88, 1.05, 1.25, and 1.32 Hz, for the same four modes.

in which contour colors measure elevations. Correspondence with analytical frequencies up to the fourth mode is excellent while using only 20 elements over the free surface.

Next, we consider a 3D version of the previous problem, with a cubic container of side $L = 1$ m. The volume of the fluid is discretized using five divisions on each direction, with a slight mesh refinement in the vertical direction, obtaining a finite element mesh of 216 nodes and $5 \times 5 \times 5$ eight-node isoparametric fluid elements. Analytical solution is computed using equation (86) and compared with numerical results in Table III.

Compared with the 2D case, it can be appreciated in Figure 13 that more complicated bidimensional sloshing modes appear over the free surface. These pertain to even and odd wavenumber combinations. Even with such a crude mesh, the first two modes and their combinations along two surface directions are correctly represented with a natural frequency error below 3%.

As a final case, the sloshing frequencies of a cylindrical rigid container of diameter $\phi = 2$ m and water height $H = 2$ m were computed. The finite element mesh is composed of 803 nodes and 640 eight-node hexahedral fluid elements, providing 16 circumferential divisions and 10 elements in the vertical direction. Mesh grading is used near the free surface.

The analytical solution for sloshing in a rigid cylinder for symmetric and antisymmetric modes can be obtained from the zeros of Bessel functions derivatives [1]. This results in the values presented in Table IV for our specific case. Comparing with numerical results, it is clear that good agreement is obtained for the first two antisymmetric modes and the first symmetric mode.

DOI: 10.1002/nme

The mode shapes and corresponding sloshing frequencies for this case are presented in Figure 14 with contour colors representing elevation. These sloshing mode shapes are more complicated than for the cubic container and thus require a more refined finite element mesh in the circumferential direction.

10.2.2. Sloshing in rigid containers: transient analysis. This example investigates the accuracy level of the finite element approximation proposed for the fluid in Section 4 by comparing it with the analytical response of a well-known benchmark [69]. The problem involves the forced sloshing of a liquid inside a rectangular 2D rigid tank subjected to harmonic horizontal base excitation. The comparison analytical solution is obtained from potential theory.

A water-filled tank has the rectangular geometry depicted in Figure 15. The height-to-base aspect ratio is $H/B = 1/2$. The forced swaying motion imposed to the tank base is sinusoidal: $x_s = a_s \cos(\omega_s t)$, where a_s is the amplitude of motion (maximum displacement of the rigid walls

Table IV. Analytical/numerical comparison of the first four sloshing frequencies for symmetric (S) and antisymmetric (AS) modes of a cylindrical container with rigid walls.

Sloshing freq.	Analytical (Hz)	Computed (Hz)
Mode (1,S)	0.98	0.99
Mode (2,S)	1.32	1.41
Mode (1,AS)	0.67	0.67
Mode (2,AS)	0.87	0.88

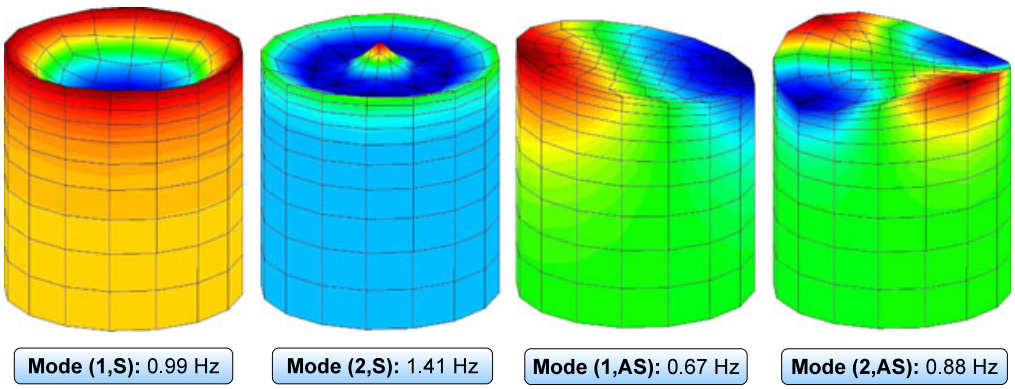

Figure 14. Symmetric and antisymmetric sloshing modes and natural frequencies in a cylindrical container with rigid walls. S, symmetric; AS, antisymmetric.

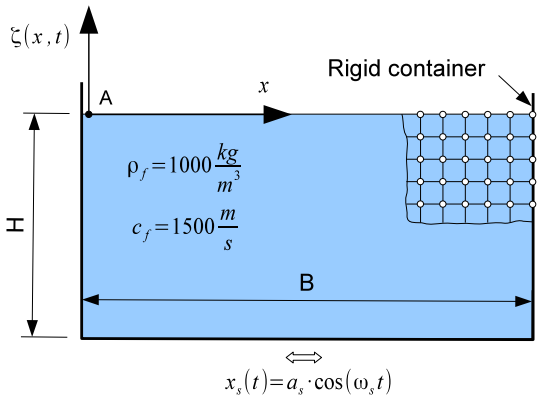

Figure 15. Model of the tank excited horizontally with prescribed harmonic motion of amplitude a_s and frequency ω_s. Time records of the free-surface elevation are obtained at the left wall of the rigid container (point A).

DOI: 10.1002/nme

from the reference configuration) and ω_s is the excitation frequency. The surface elevation $\zeta(x,t)$ is measured on the left wall of the tank ($x = 0$) and compared with analytical solutions for different forcing amplitudes and frequencies. Regular finite element grids of size 20×40 and 40×80 are used for low and high forcing frequencies, respectively.

With the use of potential theory, by solving the Laplace equation in a rectangular domain with rigid-wall boundary conditions and expanding the free-surface boundary condition into Taylor series near the mean water level $\zeta = 0$, it can be shown that the solution for the free-surface elevation can be analytically expressed as an expansion of the linear sloshing modes in the form

$$\zeta(x,t) = a_s \sum_{n=0}^{\infty} \cos(k_n x) Z_n(\omega_s t) \tag{87}$$

where $k_n = n\pi/B$ is the wave number corresponding to the nth sloshing mode and $Z_n(\omega_s t)$ are time dependent Fourier components. Using a classical perturbation approach [70], we can represent the function Z_n in the form of an asymptotic expansion with respect to the powers of the small parameter κ_s as

$$Z_n = Z_n^{(1)} + \kappa_s Z_n^{(2)} + \mathcal{O}(\kappa_s^2) \tag{88}$$

where $\kappa_s = a_s\omega_s^2/g$ is the characteristic wave steepness, which is a measure of the nonlinearity of the solution. The second-order potential theory is obtained by truncation of the second-order term in (88) and substitution in (87) to approximate surface elevation. Functions $Z_n^{(1)}$ and $Z_n^{(2)}$ are then obtained by collecting same-order terms after replacing the free-surface approximation on the second-order expanded free-surface boundary condition.

The analytical second-order solution for the free-surface profile can be finally presented as

$$\zeta(x,t) = a_s \left[\sum_{n=0}^{\infty} \cos(k_n x) Z_n^{(1)}(\omega_s t) + \left(\frac{a_s \omega_s^2}{g} \right) \sum_{n=0}^{\infty} \cos(k_n x) Z_n^{(2)}(\omega_s t) \right], \tag{89}$$

in which the definition of functions $Z_n^{(1)}$ and $Z_n^{(2)}$, expressed as products of the derivatives of the first-order solutions, can be found in [70]. By varying the applied external force through the characteristic wave steepness parameter κ_s, the free-surface behavior is examined for two different situations corresponding to before and after resonance condition, where resonance occurs when the external horizontal forcing frequency ω_s matches the natural sloshing frequency ω_n of the fluid.

Figure 16 (left column) shows the free-surface elevation at the left wall in an off-resonance region before the first natural frequency with $\omega_h/\omega_1 = 0.7$ and a small horizontal forcing amplitude $\kappa_s = 0.0036$. The second test presented in Figure 16 (right column) corresponds to an off-resonance case with forcing frequency $\omega_s/\omega_1 = 1.3$ higher than the first natural sloshing frequency and a steepness factor $\kappa_s = 0.072$. Excellent agreement between the proposed finite element approach and the second-order small perturbation theory proposed by Frandsen is found in the time history of the surface elevation for both cases.

Associated wave phase-plane orbits corresponding to those two different cases are presented in the middle plots of Figure 16. These show a linear response of the free surface with bounded orbits and increasing chaotic behavior for higher steepness parameter κ_s. Note that surface elevation is made dimensionless with respect to the forcing amplitude a_s pertaining to each case.

The lower plots of Figure 16 show power spectra of the free-surface elevations in both cases. It can be observed, for the small forcing amplitude case, that energy clusters are at two distinct frequencies, that is, at the forcing frequency and at the first sloshing frequency. In addition, for the larger forcing amplitude case, an additional third frequency ω_3 with low energy content exists, contributing to the lower numerical predicted peaks.

In summary, the proposed finite element approach provides second-order accuracy, thanks to the inclusion of the geometrical stiffness term (35). It was found that resonance and a high value of the steepness parameter $\kappa_s > 0.1$ lead to significantly nonlinear behavior. Modeling such effects would require a degree of approximation higher than the second-order degree achieved with the proposed finite element approach.

DOI: 10.1002/nme

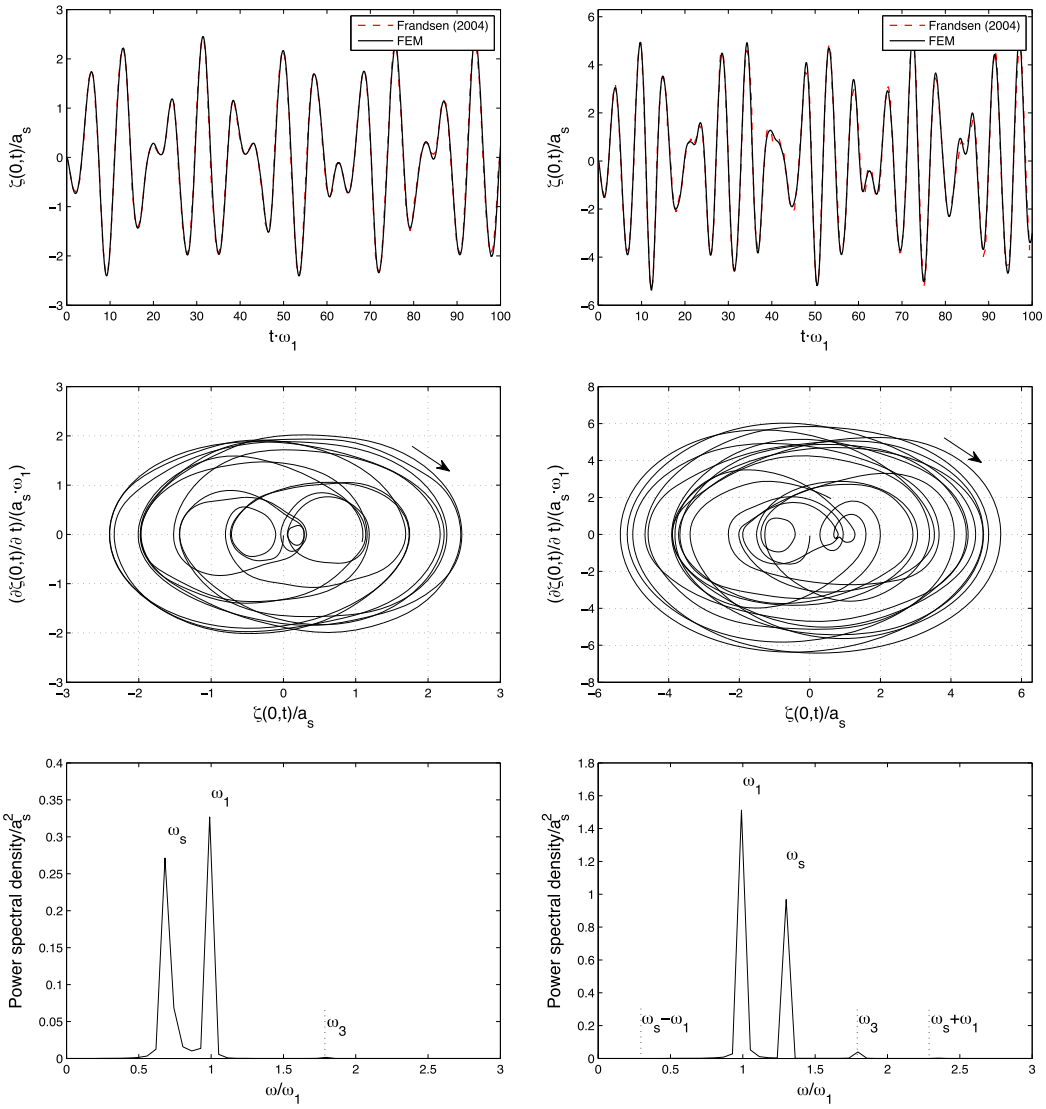

Figure 16. Free-surface elevation at the left wall of an horizontally excited rigid tank compared with the second-order theory of Frandsen [70] and wave phase-plane with spectral content of the FEM solutions. Small horizontal forcing with $\kappa_s = 0.0036$ and $\omega_s/\omega_1 = 0.7$ (left column) and higher horizontal forcing with $\kappa_s = 0.072$ and $\omega_s/\omega_1 = 1.3$ (right column). The time histories of the forced sloshing analyses are non-dimensionalized with the first natural frequency ω_1.

10.3. Sloshing in flexible containers

When the fluid container is flexible, the hydrodynamic pressure due to free-surface oscillations (slosh) causes wall deflections, which in turn alters both surface oscillation and the hydrodynamic forces on the wall. This coupling effect is studied in the next two examples for the square and cubic tanks of the previous section.

In the 2D case, represented in Figure 17, the elastic tank is modeled using a regular mesh with 30 beam elements with three DOFs per node, restricting displacements and rotation of a node located at the center of the bottom plate. The material properties of the container are $E_s = 2.1 \cdot 10^{11}$ Pa, $\nu_s = 0.3$ with density $\rho_s = 2500$ kg/m^3 and wall thickness $t_s = 2$ mm. The mode shapes and natural frequencies of the empty structure are also represented in Figure 17 up to the fourth mode.

DOI: 10.1002/nme

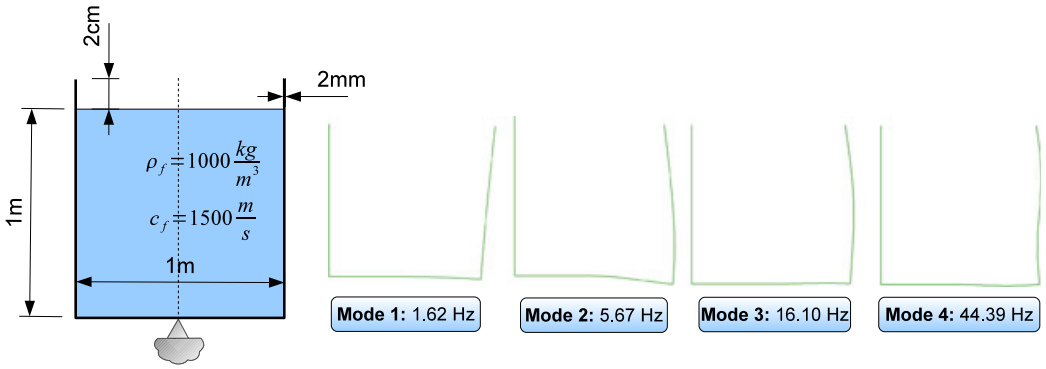

Figure 17. Dimensions of the flexible container, boundary conditions and the first four mode shapes of the structure vibrating *in vacuo*.

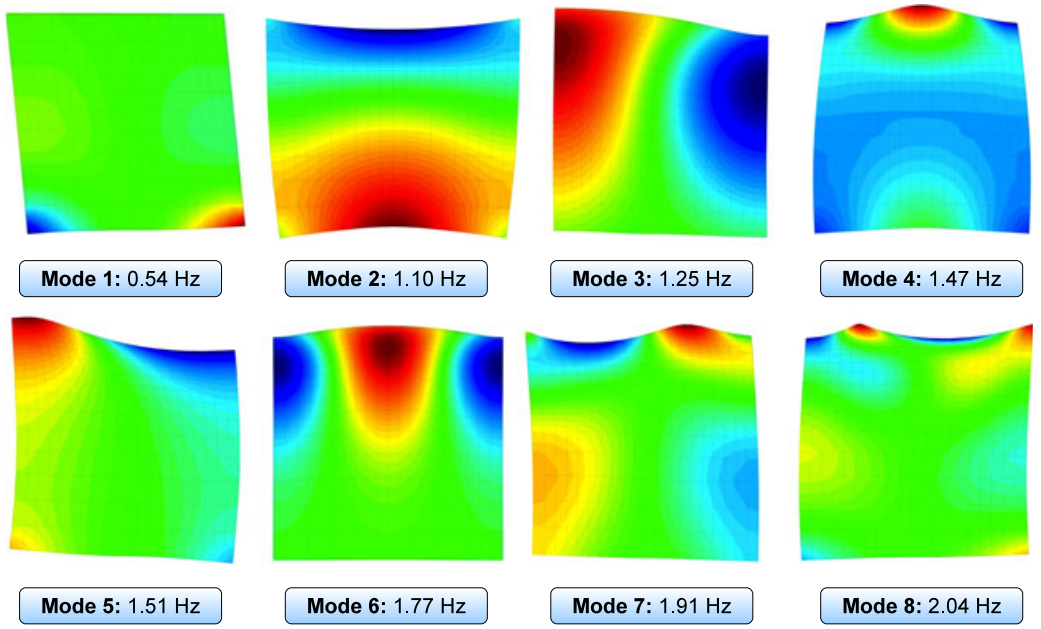

Figure 18. Coupled mode shapes of the 2D Results of the 3D sloshing problem with flexible walls. The first natural frequencies of the fluid container (dry structure) are 1.62, 5.67, 16.1, and 44.39 Hz.

The results of performing a vibration analysis of the coupled system are presented in Figure 18, reusing the same fluid mesh of the rigid-wall case. The well-known added mass effect on the first two coupled modes can be observed because structure-driven coupled modes display a lower frequency than their counterparts in the dry structure. Note that sloshing modes now appear at higher frequencies: the third coupled mode with frequency 1.25 Hz corresponds to the first analytical sloshing mode that appears at 0.88 Hz in a rigid container, and the sixth coupled mode with frequency 1.77 Hz corresponds to the second sloshing mode of 1.25 Hz. More complicated slosh patterns for the fluid are observed at higher frequencies.

In the 3D case, the vibration analysis of the cubic tank is revisited introducing six flexible walls for the container. The mesh used for the fluid is the same used in the rigid-wall case. The structure mesh is composed of 125 quadrilateral plate elements with three DOFs per node: the normal displacement and two in-plane rotations. Boundary conditions are somewhat different than those in the

DOI: 10.1002/nme

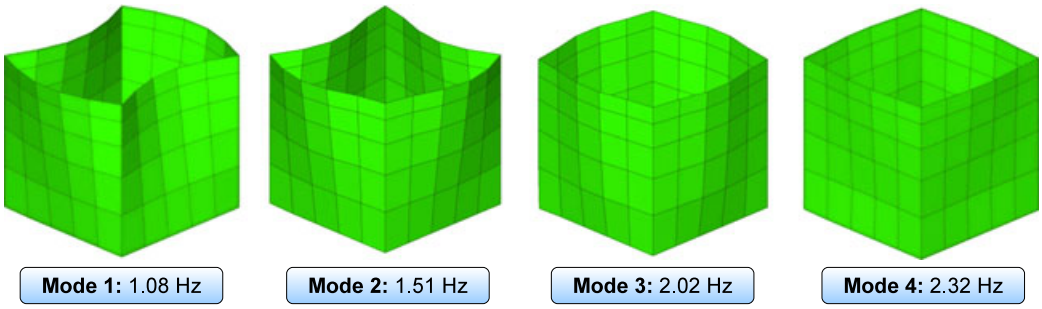

Figure 19. Mode shapes and natural frequencies of the cubic container vibrating *in vacuo*.

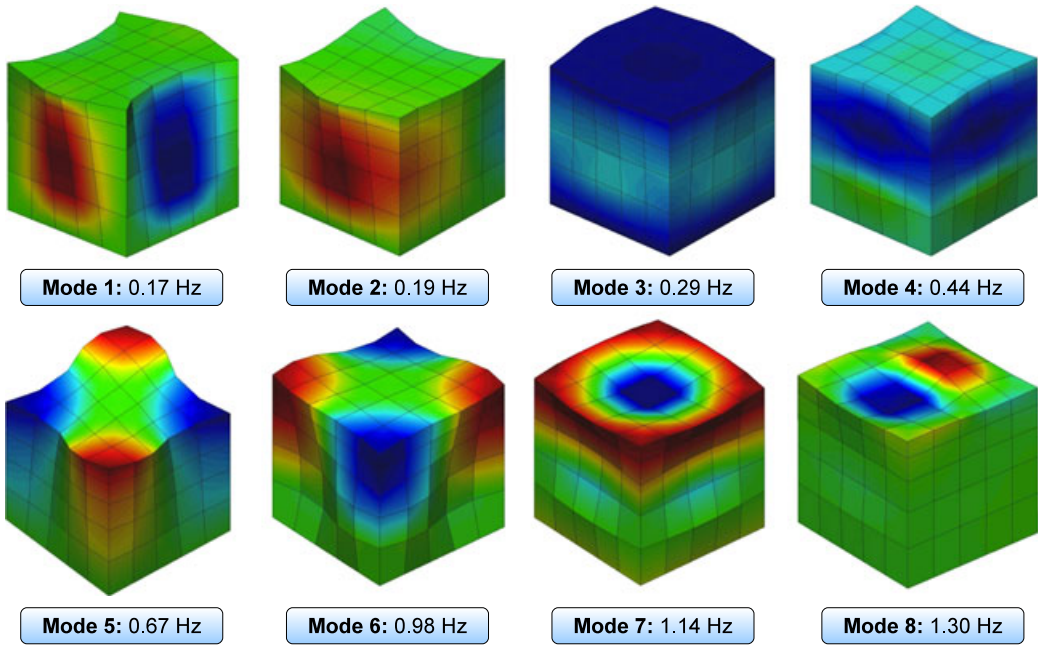

Figure 20. Coupled mode shapes for the fluid contained in a cubic tank with corresponding natural frequencies.

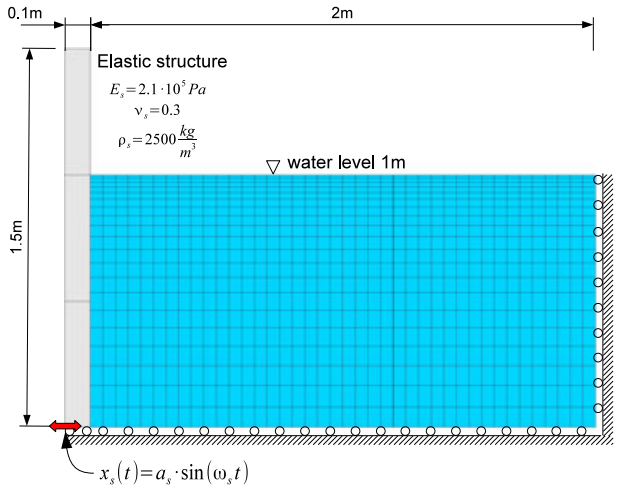

Figure 21. Wave generator: geometry, boundary conditions, and material properties.

DOI: 10.1002/nme

previous example, with each face of the tank being considered as a simply supported plate. Structural material properties are $E_s = 210$ GPa, $\nu_s = 0.3$, and $\rho_s = 2500$ kg/m^3, with a plate thickness $t_s = 2$ mm.

The natural frequencies and mode shapes of the dry structure can be found in Figure 19 and the coupled mode shapes with their corresponding frequencies in Figure 20. The first four coupled modes obtained are structure-driven modes exhibiting added mass effect, with the third one associated with the vibration of the bottom plate. Sloshing appears in the form of coupled modes after the fourth frequency.

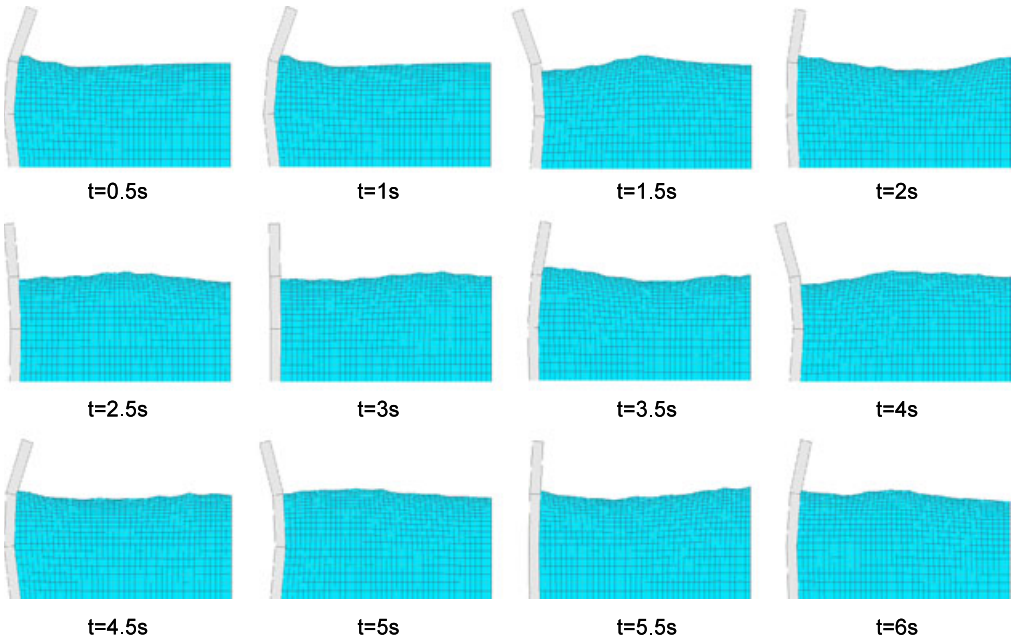

Figure 22. Wave generator: deformed configurations at different time steps.

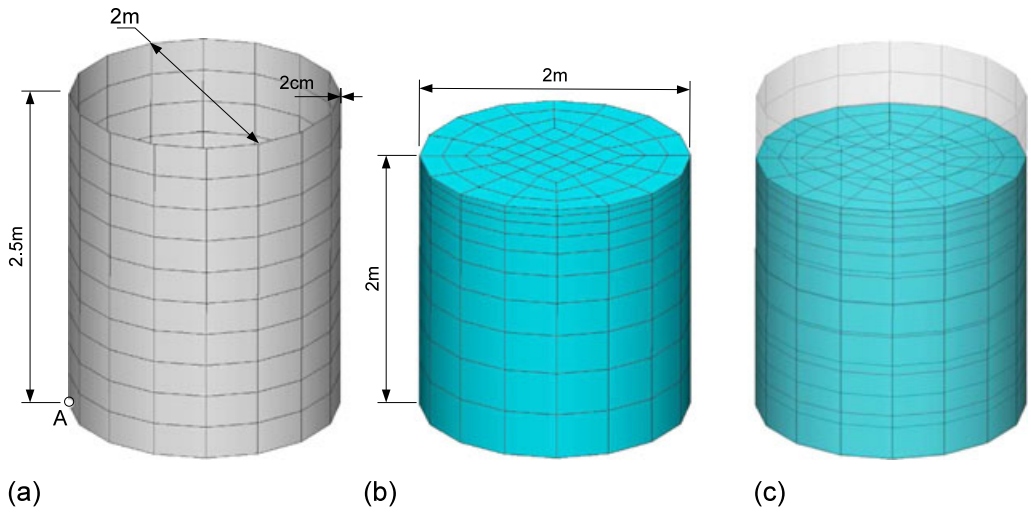

Figure 23. Dimensions and meshes of the (a) cylindrical container, (b) internal fluid, and (c) coupled system presenting non-matching interfaces.

DOI: 10.1002/nme

10.4. Wave generator

This example is devised to demonstrate that the proposed interfacing strategy can handle scenarios with drastic mesh transitions from structure to fluid without further modifications. A flexible structure modeled using only three quadrilateral elements, as represented in Figure 21, is used to generate waves on a rectangular basin by imposing a harmonic horizontal motion $x_s(t) = a_s \sin(\omega_s t)$ at the left bottom node of the structure with frequency $\omega_s = 6.28$ rad/s and amplitude $a_s = 5$ cm. Fluid and structure have material properties, boundary conditions, and dimensions given in Figure 21. Meshes are composed of three plane-strain quadrilateral elements for the structure and 800 quadrilateral fluid elements with 861 nodes for the fluid.

Dynamic response calculations are carried out by direct time integration of the equations of motion (82) with the Trapezoidal Rule equivalent Newmark method, using a time step of $\Delta t = 1 \cdot 10^{-2}$ s. Figure 22 depicts induced fluid wave histories, showing that the dynamic interface-frame

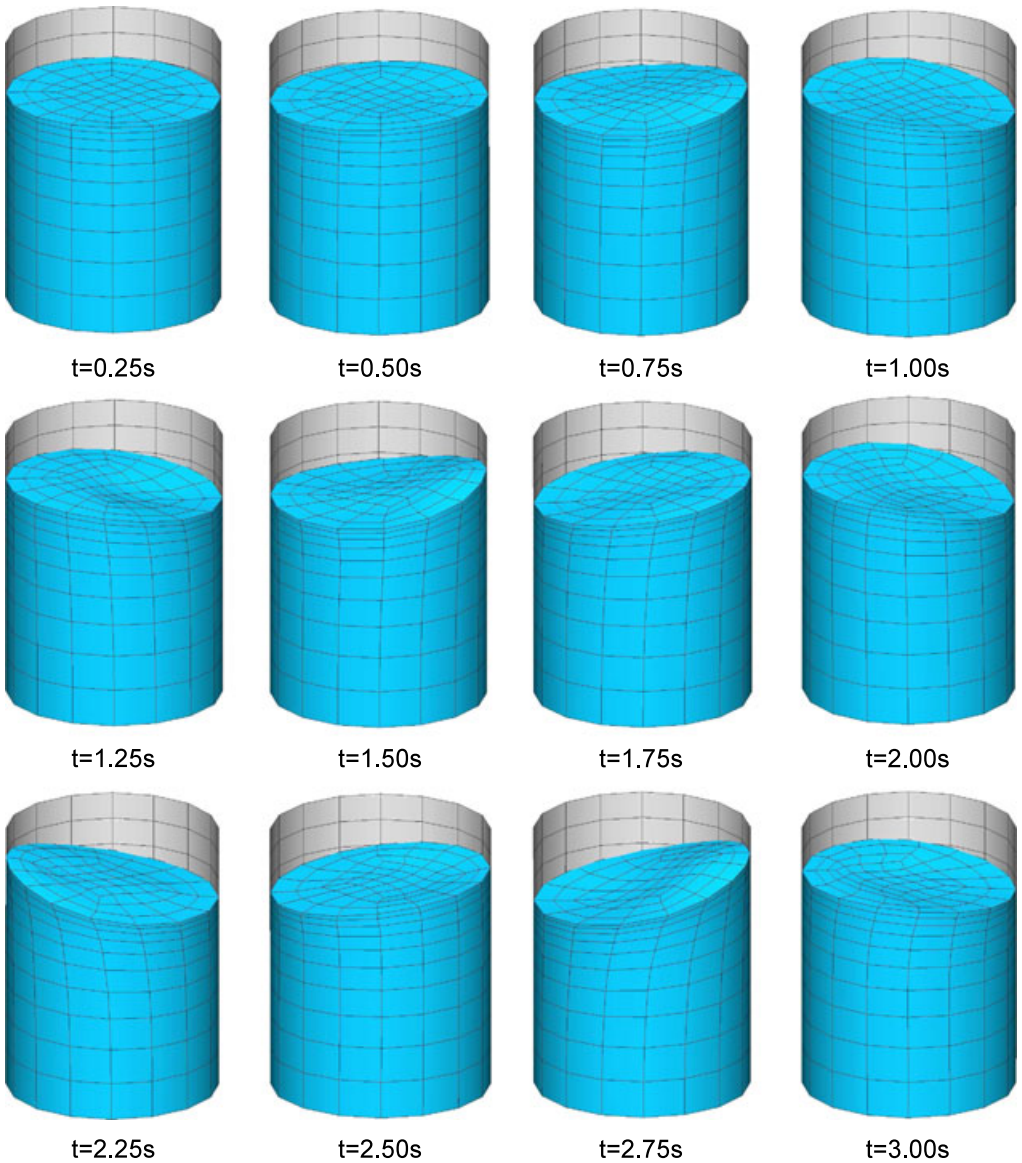

Figure 24. Cylindrical container: deformed configurations for different time steps. Half cylinder is removed for a clear visualization of the free-surface evolution.

DOI: 10.1002/nme

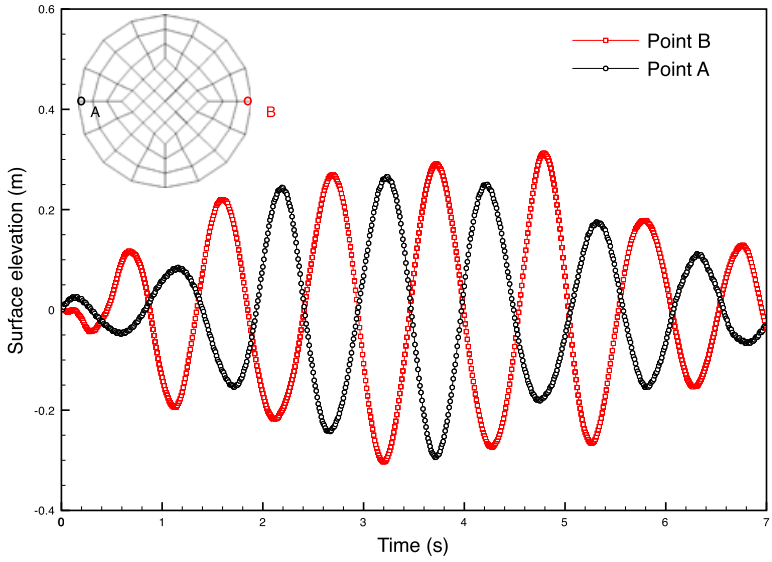

Figure 25. Cylindrical container: evolution of the free-surface elevation at opposite points near the wall aligned with the direction of imposed motion.

approach can handle contact of sharp edges with no difficulties. These encouraging results underline the interface strategy behind the combination of LLMs and ZMR techniques, on the basis of the interface construction scheme presented in Section 8.

10.5. Cylindrical container

In the last example, a cylindrical container partially filled with water up to a height $H = 2$ m is subject to a forced motion in the horizontal plane. The container is modeled using a regular mesh of 160 four-node structural shell elements with 176 nodes and six DOFs per node. The structural properties are $E_s = 2.1 \cdot 10^9$ Pa, $\nu_s = 0.3$, density $\rho_s = 2500$ kg/m^3, and shell thickness $t_s = 2$ mm. All the nodes of the shell structure laying on the floor are allowed to move freely in the X–Y plane except point A (Figure 23), which is subjected to a sinusoidal forced motion in the X-direction of amplitude $a_s = 2$ cm and frequency $\omega_s = 1$ Hz.

The interior fluid, with properties $\rho_f = 1000$ kg/m^3 and $c_f = 1500$ m/s, is modeled using 640 hexahedral finite elements and 803 nodes with three DOFs per node, exactly the same mesh used for the rigid case. A spatial discretization detail is shown in Figure 23 to emphasize the presence of non-matching between fluid and structure meshes. The transient response simulation was performed by direct integration of (82) using the Trapezoidal Rule equivalent Newmark's scheme, with time step $\Delta t = 1 \cdot 10^{-2}$ s.

The pictures in Figure 24 show the evolution in time of the free-surface due to the prescribed swaying motion imposed to the tank. The solution combines stretching of the container walls in the horizontal direction and large amplitude waves in the free surface with a swirl effect. Note that, when the fluid free-surface runs up and down the walls of the container, temporal activation and deactivation of structural interface nodes take place.

Time history of free-surface elevation is given in Figure 25 for two points near the wall. Points A and B are aligned with the direction of external excitation.

11. CONCLUSIONS

The main objective of the paper is to demonstrate the range of applicability of the partitioned FSI formulation proposed by Park *et al.* [35] for the simulation of structures that experience significant FSI effects with coupled acoustic and gravity waves, using 2D and 3D models. Theoretical and

DOI: 10.1002/nme

implementation issues behind the techniques proposed in [35] are reviewed, extended and explained in detail as appropriate to understand its possibilities. Also, additional theory topics are included, *viz.*, the treatment of fluid quasi-incompressiblity, procedures for interfacing non-matching meshes in the case of inviscid fluids and treatment of the interface using LLMs.

A fully implicit response analysis strategy for FSI has been presented that is able to represent correctly acoustic and gravitational effects in the fluid. The numerical examples are provided to illustrate its accuracy, robustness, and efficiency. The proposed computational framework allows the independent discretization of fluid and structure, combined with a unique discretization for the interface that passes the force patch test and follows the fluid and structure interfaces during their relative motion. The strategy seems well suited for the modeling of internal fluids that exhibit free surface and interact with flexible containers.

ACKNOWLEDGEMENTS

The research reported in this paper has been supported by the World Class University (WCU) Program through the Korea Science and Engineering Foundation funded by the Ministry of Education, Science and Technology, Korea (Grant Number R31-2008-000-10045-0). J. A. González has been partially supported by the project *Proyectos Investigación de Excelencia 2008, Consejeria de Innovación Ciencia y Empresa, Junta de Andalucía, Spain*, with contract number P08-TEP-03804.

REFERENCES

1. Ibrahim RA. *Liquid Sloshing Dynamics: Theory and Applications*. Cambridge University Press: Cambridge, UK, 2005.
2. Hough SS. The oscillations of a rotating ellipsoidal shell containing fluid. *Philosophical Transactions of the Royal Society of London* 1895; **186**:469–506.
3. Abramson HN. The Dynamic Behavior of Liquids in Moving Containers, 1966. NASA SP-106.
4. Faltinsen OM, Timokha AM. *Sloshing*. Cambridge University Press: Cambridge, UK, 2009.
5. Morand HJP, Ohayon R. *Fluid Structure Interaction: Applied Numerical Methods*. John Wiley & Sons: New York, 1995.
6. Abramson HN. Dynamic behavior of liquids in moving containers. *Applied Mechanics Reviews* 1963; **16**:501–506.
7. Cariou A, Casella G. Liquid sloshing in ship tanks: a comparative study of numerical simulation. *Marine Structures* 1999; **12**:183–198.
8. Rebouillat S, Liksonov D. Fluid–structure interaction in partially filled liquid containers: a comparative review of numerical approaches. *Computers & Fluids* 2010; **39**:739–746.
9. Haroun MA, Tayel MA. Axi-symmetrical vibrations of tanks—numerical. *Journal of Engineering Mechanics, ASCE* 1985; **111**:329–345.
10. Haroun MA, Tayel MA. Axi-symmetrical vibrations of tanks—analytical. *Journal of Engineering Mechanics, ASCE* 1985; **111**:346–358.
11. Abe K. R-adaptive boundary element method for unsteady free-surface flow analysis. *International Journal for Numerical Methods in Engineering* 1996; **39**:2769–2787.
12. Donescu P, Virgin LN. An implicit boundary element solution with consistent linearization for free surface flows and non-linear fluid–structure interaction of floating bodies. *International Journal for Numerical Methods in Engineering* 2001; **51**:379–412.
13. Firouz-Abadi RD, Haddadpour H, Noorian MA, Ghasemi M. A 3D BEM model for liquid sloshing in baffled tanks. *International Journal for Numerical Methods in Engineering* 2008; **76**:1419–1433.
14. Gedikli A, Erguven ME. Evaluation of sloshing problem by variational boundary element method. *Engineering Analysis with Boundary Elements* 2003; **27**:935–943.
15. Iseki T, Shinkai A, Nakatake K. Boundary element analysis of 3-dimensional sloshing problem by using cubic spline element. *Naval Architect (Japan)* 1989; **166**:355–362.
16. Nakayama T, Washizu K. The boundary element method applied to the analysis of two-dimensional nonlinear sloshing problems. *International Journal for Numerical Methods in Engineering* 1981; **17**:1631–1646.
17. Le Tallec P, Mouro J J. Fluid structure interaction with large structural displacements. *Computer Methods in Applied Mechanics and Engineering* 2001; **190**:3039–3068.
18. Navti SE, Ravindran K, Taylor C, Lewis RW. Finite element modelling of surface tension effects using a Lagrangian–Eulerian kinematic description. *Computer Methods in Applied Mechanics and Engineering* 1997; **147**:41–60.
19. Soulaimani A, Saad Y. An arbitrary Lagrangian–Eulerian finite element method for solving three-dimensional free surface flows. *Computer Methods in Applied Mechanics and Engineering* 1998; **147**:79–106.

DOI: 10.1002/nme

20. Tezduyar TE, Behr M, Liou J. A new strategy for finite element computations involving moving boundaries and interfaces - The deforming-spatial-domain/space–time procedure: I. The concept and the preliminary numerical tests. *Computer Methods in Applied Mechanics and Engineering* 1992; **94**:339–351.
21. Wall WA, Genkinger S, Ramm E. A strong coupling partitioned approach for fluid–structure interaction with free surfaces. *Computers & Fluids* 2007; **36**:169–183.
22. Okamoto T, Kawahara M. Two-dimensional sloshing analysis by Lagrangian finite element method. *International Journal for Numerical Methods in Fluids* 1990; **11**:453–477.
23. Oñate E, Garcia JA. Finite element method for fluid–structure interaction with surface waves using a finite calculus formulation. *Computer Methods in Applied Mechanics and Engineering* 2001; **191**:635–660.
24. Radovitzky R, Ortiz M. Lagrangian finite element analysis of Newtonian fluid flows. *International Journal for Numerical Methods in Engineering* 1998; **43**:607–619.
25. Ramaswamy, Kawahara M, Nakayama T. Lagrangian finite element method for the analysis of two-dimensional sloshing problems. *International Journal for Numerical Methods in Fluids* 1986; **6**:659–670.
26. Bennett A. *Lagrangian Fluid Dynamics*. Cambridge University Press: Cambridge, UK, 2006.
27. Mead JL. The shallow water equations in Lagrangian coordinates. *Journal of Computational Physics* 2004; **200**:654–669.
28. Chen YG, Djidjeli K, Price WG. Numerical simulation of liquid sloshing phenomena in partially filled containers. *Computers & Fluids* 2009; **38**:830–842.
29. Bathe KJ, Zhang H. Finite element developments for general fluid flows with structural interactions. *International Journal for Numerical Methods in Engineering* 2004; **60**:213–232.
30. Degroote J, Bathe KJ, Vierendeels J. Performance of a new partitioned procedure versus a monolithic procedure in fluid–structure interaction. *Computers & Structures* 2009; **87**:793–801.
31. Felippa CA, Ohayon R. Mixed variational formulation of finite element analysis of acoustoelastic/slosh fluid–structure interaction. *Journal of Fluids and Structures* 1990; **4**:35–57.
32. Legay A, Chessa J, Belytschko T. An Eulerian-Lagrangian method for fluid–structure interaction based on level sets. *Computer Methods in Applied Mechanics and Engineering* 2006; **195**:2070–2087.
33. Matthies H, Steindorf J. Partitioned strong coupling algorithms for fluid–structure interaction. *Computers and Structures* 2003; **81**:805–812.
34. Park KC, Felippa CA, Ohayon R. Partitioned formulation of internal fluid–structure interaction problems by localized lagrange multipliers. *Computer Methods in Applied Mechanics and Engineering* 2001; **190**:2989–3007.
35. Park KC, Ohayon R, Felippa CA, González JA. Partitioned formulation of internal and gravity waves interacting with flexible structures. *Computer Methods in Applied Mechanics and Engineering* 2010; **199**:723–733.
36. Wall WA, Mok DP, Schmidt J, Ramm E. Partitioned analysis of transient nonlinear fluid structure interaction problems including free surface effects. In *Multifield Problems: State of the Art*, Sandig A-M, Schiehlen W, Wendland WL (eds). Springer: Germany, 2000; 159–166.
37. Park KC, Felippa CA. A variational framework for solution method developments in structural mechanics. *Journal of Applied Mechanics* 1998; **65**:242–249.
38. Park KC, Felippa CA. A variational principle for the formulation of partitioned structural systems. *International Journal for Numerical Methods in Engineering* 2000; **47**:395–418.
39. Park KC, Felippa CA, Gumaste U. A localized version of the method of lagrange multipliers and its applications. *Computational Mechanics* 2000; **24**:476–490.
40. Andrianarison O, Ohayon R. Compressibility and gravity effects in internal fluid–structure vibrations: basic equations and appropriate variational formulations. *Computer Methods in Applied Mechanics and Engineering* 2006; **195**:1958–1972.
41. Andrianarison O, Ohayon R. Reduced models for modal analysis of fluid–structure systems taking into account compressibility and gravity effects. *Computer Methods in Applied Mechanics and Engineering* 2006; **195**: 5656–5672.
42. Bermúdez A, Hervella-Nieto L, Rodriguez R. Finite element computation of three-dimensional elastoacoustic vibrations. *Journal of Sound and Vibration* 1999; **219**:279–306.
43. Bermúdez A, Hervella-Nieto L, Rodríguez R. Finite element computation of the vibrations of a plate–fluid system with interface damping. *Computer Methods in Applied Mechanics and Engineering* 2001; **190**:3021–3038.
44. Bermúdez A, Rodríguez R. Finite element computation of the vibration modes of a fluid–solid system. *Computer Methods in Applied Mechanics and Engineering* 1994; **119**:355–370.
45. Ohayon R. Reduced symmetric models for modal analysis of internal structural-acoustic and hydroelastic-sloshing systems. *Computer Methods in Applied Mechanics and Engineering* 2001; **190**:3009–3019.
46. Lighthill J. *Waves in Fluids*. Cambridge University Press: Cambridge, UK, 1978.
47. Kanok-Nukulchai W, Tam B. Structure–fluid interaction model of tuned liquid dampers. *International Journal for Numerical Methods in Engineering* 1999; **46**:1541–1558.
48. Kishor DK, Gopalakrishnan S, Ganguli R. Three-dimensional sloshing: a consistent finite element approach. *International Journal for Numerical Methods in Fluids* 2011; **66**:345–376.
49. Park WS, Yun C-B, Pyun C. Infinite elements for 3-dimensional wave–structure interaction problems. *Engineering Structures* 1992; **14**:335–346.
50. Parrinello F, Borino G. Lagrangian finite element modelling of dam–fluid interaction: accurate absorbing boundary conditions. *Computers & Structures* 2007; **85**:932–943.

DOI: 10.1002/nme

51. Simo J, Taylor R. Quasi-incompressible finite elasticity in principal stretches. Continuum basis and numerical algorithms. *Computer Methods in Applied Mechanics and Engineering* 1991; **85**:273–310.
52. Simo J, Taylor R, Pister K. Variational and projection methods for the volume constraint in finite deformation elasto-plasticity. *Computer Methods in Applied Mechanics and Engineering* 1985; **51**:177–208.
53. Bathe KJ. The inf–sup condition and its evaluation for mixed finite element methods. *Computers & structures* 2001; **79**:243–252.
54. Chapelle D, Bathe K. The inf–sup test. *Computers & structures* 1993; **47**:537–545.
55. Washizu K. *Variational Methods in Elasticity and Plasticity*. Pergamon Press: New York, 1972.
56. de Veubeke BMF. Diffusion des inconnues hyperstatiques dans les voilures à longeron couplés. *Bulletin du Service Technique de l'Aéronautique* 1951; **24**:1–56.
57. Bonet J, Wood RD. *Nonlinear Continuum Mechanics for Finite Element Analysis*, 2nd ed. Cambridge University Press: Cambridge, UK, 2008.
58. Felippa CA. A survey of parametrized variational principles and applications to computational mechanics. *Computer Methods in Applied Mechanics and Engineering* 1994; **113**:109–139.
59. González JA, Park KC, Felippa CA. Partitioned formulation of frictional contact problems using localized Lagrange multipliers. *Communications in Numerical Methods in Engineering* 2005; **22**:319–333.
60. González JA, Park KC, Felippa CA. A formulation based on localized Lagrange multipliers for BEM–FEM coupling in contact problems. *Computer Methods in Applied Mechanics and Engineering* 2008; **197**:623–640.
61. Rebel G, Park KC, Felippa CA. A contact formulation based on localized lagrange multipliers: formulation and application to two-dimensional problems. *International Journal for Numerical Methods in Engineering* 2002; **54**:263–297.
62. Park KC, Felippa C, Rebel G. Interfacing nonmatching FEM meshes: the zero moment rule. In *Trends in Computational Structural Mechanics*, Wall W, Bletzinger K, Schweizer K (eds). CIMNE: Barcelona, Spain, 2001.
63. Ross MR. Coupling and Simulation of Acoustic Fluid–Structure Interaction Systems Using Localized Lagrange Multipliers. *PhD thesis*, University of Colorado, 2006.
64. Ross MR, Felippa CA, Park KC, Sprague MA. Treatment of acoustic fluid–structure interaction by localized lagrange multipliers: formulation. *Computer Methods in Applied Mechanics and Engineering* 2008; **197**:3057–3079.
65. Ross MR, Sprague MA, Felippa CA, Park K. Treatment of acoustic fluid–structure interaction by localized lagrange multipliers and comparison to alternative interface-coupling methods. *Computer Methods in Applied Mechanics and Engineering* 2009; **198**:986–1005.
66. Park KC, Felippa CA, Rebel G. A simple algorithm for localized construction of non-matching structural interfaces. *International Journal for Numerical Methods in Engineering* 2002; **53**:2117–2142.
67. Crisfield MA. Re-visiting the contact patch test. *International Journal for Numerical Methods in Engineering* 2000; **48**:435–449.
68. Zienkiewicz O, Taylor R. *The Finite Element Method: Basic Formulation and Linear Problems*, 4th ed., Vol. 1. McGraw-Hill Book Company: London, 1989.
69. Colagrossi A, Palladino F, Greco M, Lugni C, Faltinsen O. Experimental and numerical investigation of 2D sloshing: scenarios near the critical filling depth. *21st IWWWFB*, Loughborough, UK, 2006.
70. Frandsen J. Sloshing motions in excited tanks. *Journal of Computational Physics* 2004; **196**:53–87.

DOI: 10.1002/nme